BRNO UNIVERSITY OF TECHNOLOGY
VYSOKÉ UČENÍ TECHNICKÉ V BRNĚ

FACULTY OF MECHANICAL ENGINEERING
FAKULTA STROJNÍHO INŽENÝRSTVÍ

INSTITUTE OF PHYSICAL ENGINEERING
ÚSTAV FYZIKÁLNÍHO INŽENÝRSTVÍ

EFFECT OF PHYSICAL FLUID PROPERTIES ON HEAT TRANSFER EFFICIENCY IN TURBULENT RAYLEIGH-BÉNARD CONVECTION

VLIV FYZIKÁLNÍCH VLASTNOSTÍ TEKUTINY NA EFEKTIVITU TEPELNÉHO PŘENOSU TURBULENTNÍ RAYLEIGHOVOU-BÉNARDOVOU KONVEKCÍ

MASTER'S THESIS
DIPLOMOVÁ PRÁCE

AUTHOR AUTOR PRÁCE	Bc. TOMÁŠ VĚŽNÍK
SUPERVISOR VEDOUCÍ PRÁCE	Ing. PAVEL URBAN, Ph.D.

BRNO 2021

INSTITUTE OF SCIENTIFIC INSTRUMENTS
The Czech Academy of Sciences

This Master's Thesis was elaborated at the

Institute of Scientific Instruments of the CAS, v. v. i.

under supervision of:
Ing. Pavel Urban, Ph.D.

Assignment Master's Thesis

Institut:	Institute of Physical Engineering
Student:	**Bc. Tomáš Věžník**
Degree programm:	Physical Engineering and Nanotechnology
Branch:	no specialisation
Supervisor:	**Ing. Pavel Urban, Ph.D.**
Academic year:	2020/21

As provided for by the Act No. 111/98 Coll. on higher education institutions and the BUT Study and Examination Regulations, the director of the Institute hereby assigns the following topic of Master's Thesis:

Effect of physical fluid properties on heat transfer efficiency in turbulent Rayleigh–Bénard convection

Brief Description:

Natural buoyancy–driven turbulent convection plays a vital role in heat and mass transfer on large–scales in Nature, such as the circulation in the atmosphere or in the oceans, the flows under the surface of stars or in diverse branches of industry. Laboratory and numerical modelling of natural convection is possible on the base of a simplified physical model system – Rayleigh–Bénard convection (RBC). Such model is realized in a layer of working fluid often confined to a cylindrical experimental cell which is heated from bellow and cooled from above with a vertical temperature gradient parallel to gravity. One of the most discussed topics in the field of RBC is the existence of its ultimate regime theoretically predicted by Kraichnan in 1960s. Confirmation of such a regime would be of great importance for understanding many natural and practical phenomena mentioned above, as the heat transfer efficiency rises significantly. Observation of the transition to the ultimate regime has been claimed several times – initially in the Grenoble cryogenic helium experiments and more recently also in the Göttingen room temperature SF6 experiments. The experimental work at Institute of Scientific Instruments CAS (ISI Brno) sheds new light on this issue by pointing out that the effect of temperature dependent properties of the working fluid increases the heat transfer efficiency and thus the important issue of the transition to the ultimate regime of RBC remains open.

Master's Thesis goals:

The aim is to perform experiments on heat transfer efficiency at high intensity of turbulent convection (Rayleigh number up to 1E15) using working points (temperature and pressure) in the phase diagram of cold helium gas (4He) close to the critical point (5.2 K, 227 kPa) and/or critical isochore. Finally, the influence of working point positions in the 4He phase diagram on heat transfer efficiency will be analysed in details. The experiment will take place at IS Brno using of the existing ConEV (Convection Experimental Vessel) experimental apparatus, specially designed for this purpose.

Recommended bibliography:

TRITTON, D.J. Physical Fluid Dynamics. 2 ed. Oxford: Clarendon Press, 1988. ISBN 0-19-854493-6.

KRAICHNAN, Robert H. Turbulent Thermal Convection at Arbitrary Prandtl Number. Physics of Fluids. 1962, 5(11). ISSN 00319171. Dostupné z: doi:10.1063/1.1706533

CHAVANNE, X., F. CHILLÀ, B. CASTAING, B. HÉBRAL, B. CHABAUD a J. CHAUSSY. Observation of the Ultimate Regime in Rayleigh-Bénard Convection. Physical Review Letters. 1997, 79(19), 3648-3651. ISSN 0031-9007. Dostupné z: doi:10.1103/PhysRevLett.79.3648

HE, Xiaozhou, Denis FUNFSCHILLING, Holger NOBACH, Eberhard BODENSCHATZ, Guenter AHLERS a J. CHAUSSY. Transition to the Ultimate State of Turbulent Rayleigh-Bénard Convection. Physical Review Letters. 2012, 108(2), 3648-3651. ISSN 0031-9007. Dostupné z: doi:10.1103/PhysRevLett.108.024502

SKRBEK, L., P. URBAN, Holger NOBACH, Eberhard BODENSCHATZ, Guenter AHLERS a J. CHAUSSY. Has the ultimate state of turbulent thermal convection been observed? Journal of Fluid Mechanics. 2015, 785(2), 270-282. ISSN 0022-1120. Dostupné z: doi:10.1017/jfm.2015.638

URBAN, P., P. HANZELKA, T. KRÁLÍK, M. MACEK, V. MUSILOVÁ a L. SKRBEK. Elusive transition to the ultimate regime of turbulent Rayleigh-Bénard convection. Physical Review E. 2019, 99(1), 270-282. ISSN 2470-0045. Dostupné z: doi:10.1103/PhysRevE.99.011101

Deadline for submission Master's Thesis is given by the Schedule of the Academic year 2020/21

In Brno,

L. S.

prof. RNDr. Tomáš Šikola, CSc. Director of the Institute	doc. Ing. Jaroslav Katolický, Ph.D. FME dean

Abstract
We performed experiments with turbulent Rayleigh-Bénard convection in cryogenic helium gas in a wide range of Rayleigh numbers $10^8 < Ra < 6 \times 10^{12}$ to improve our understanding of effects related to (i) a variation of fluid properties with pressure and temperature within the convecting fluid, the so-called non-Oberbeck-Boussinesq (NOB) effects, and (ii) thermal boundary conditions of the convection cell at the bottom (heating) and top (cooling) plates. The most important NOB effects are the asymmetry in properties of the boundary layers (BL) and the influence on the heat transfer efficiency (Nusselt number Nu). The results of this thesis correlate the influence on heat transfer efficiency with varying properties of the boundary layers and also with the position of working points in the p-T phase diagram of helium. On the other hand, the stability of temperatures of the heating/cooling plates determining the type of boundary conditions for the system (constant temperature vs. constant heat flux) led to no detectable differences in Nu. Finally, Reynolds numbers Re related to large-scale circulation (LSC) inside the cell were evaluated based on a statistical analysis of the bottom plate temperature fluctuations and compared to the corresponding values of Reynolds number evaluated from the cell center sensors. We found that it is possible to assess the Re number from thermal fluctuations of the bottom plate at high Ra. For $Ra < 10^{10}$, vanishing of the first peak in the auto-correlation function of the plate temperature indicate the weakening interaction of LSC with the bottom plate via the BL.

Abstrakt
Byla provedena měření turbulentní Rayleighovy-Bénardovy konvekce v kryogenním heliu v rozsahu Rayleighových čísel $10^8 < Ra < 6 \cdot 10^{12}$ s cílem zlepšit pochopení dějů spojených s (i) proměnností na tlaku a teplotě závisejících vlastností tekutiny uvnitř konvekce, tzv. ne-Oberbeckovy-Boussinesquovy (NOB) efekty, a s (ii) okrajovými podmínkami v konvekční cele na spodní (topné) a horní (chladící) desce. Nejdůležitější efekty jsou asymetrie v mezních vrstvách (BL) vznikající na základě proměnnosti vlastností tekutiny s teplotou a vliv na efektivitu přenosu tepla (Nusseltevo číslo Nu). Výsledky této práce dávají do souvislosti efektivitu přenosu tepla s měnícími se vlastnostmi mezní vrstvy a také s pozicí měřených bodů ve fázovém p-T diagramu helia. Na druhou stranu, stabilita teploty topné/chladící desky určující typ okrajové podmínky systému (konstantní teplota vs. konstantní tepelný tok) vede k zanedbatelnému vlivu na efektivitu přenosu tepla. Na závěr bylo na základě statistické analýzy teplotních fluktuací na spodní desce vyhodnoceno Reynoldsovo číslo Re vztahující se k cirkulačnímu pohybu tekutiny v cele (LSC) a porovnáno s odpovídajícími hodnotami vyhodnocenými ze záznamu teploty uprostřed cely. Zjistili jsme, že je možné získat Re z teplotních fluktuací na spodní desce pro vysoká Ra. Vymizení prvního maxima v autokorelační funkci teploty spodní desky pro $Ra < 10^{10}$ ukazuje na slábnoucí interakci LSC se spodní deskou protřednictvím BL.

Keywords
Rayleigh-Bénard convection, non-Oberbeck-Boussinesq effects, boundary conditions, Reynolds number

Klíčová slova
Rayleighova-Bénardova konvekce, ne-Oberbeckovy-Boussinesquovy efekty, okrajové podmínky, Reynoldsovo číslo

VĚŽNÍK, T.*Effect of physical fluid properties on heat transfer efficiency in turbulent Rayleigh-Bénard convection.* Brno: Vysoké učení technické v Brně, Faculty of Mechanical Engineering, 2021. ?? s. Vedoucí Ing. Pavel Urban, Ph.D.

I declare that this master thesis is based on my own work, led by my supervisor Ing. Pavel Urban, Ph.D., and all utilized sources are properly listed in the bibliography. I proclaim that all presented information is accurate.

Bc. Tomáš Věžník

I would first like to thank my supervisor Pavel Urban for his valuable help with this thesis and also big support in the measurement. I would also like to thank Tomáš Králík for his software support and to Věra Musilová and Michal Macek for stimulating discussion.

We acknowledge the support of this research by the Czech Science Foundation under the project GAČR 20-00918S.

Bc. Tomáš Věžník

Contents

Introduction 3

1 Theory 7
  1.1 Equations describing RBC . . . 7
  1.2 Nondimensionalization . . . 7
  1.3 Heat transfer efficiency . . . 8
  1.4 Boundary conditions . . . 11
  1.5 Non-Oberbeck-Boussinesq effects . . . 12
  1.6 Large scale circulation dynamics . . . 14

2 Goals of the Thesis 17
  2.1 Helium as a working fluid . . . 17

3 Experimental set-up 19
  3.1 Helium cryostat and convection cell . . . 19
  3.2 Temperature sensors in the convection cell . . . 20
  3.3 Data measurement . . . 22
  3.4 PID regulation . . . 22
  3.5 Experimental protocol . . . 24

4 Results 25
  4.1 Evaluation of non-Oberbeck-Boussinesq effects . . . 26
  4.2 Effect of thermal boundary conditions . . . 30
  4.3 Large scale flow . . . 33

5 Summary and conclusions 39

List of symbols, physical constants and abbreviations 44

Appendix 48

Introduction

Natural convection, after so many years of study, is still a rich field of research. Its nonlinearity, dependence on so many variables, complexness, and yet so commonness (usualness) in everyday life (in the atmosphere, ocean, room, above the cup of hot tea...) is so stunning, challenging people in the theory, simulations, and experiments. In this sense, *natural* means that the fluid flow is generated only by density differences in the fluid.

Rayleigh-Bénard convection (RBC) is a simplified model of natural convection realized in the infinite horizontal layer of fluid with thickness L, heated from below, and cooled from above. The key role in the study of Rayleigh-Bénard convection is to find how effectively is the heat transferred. This is essential for example in the understanding of the Earth's surface cooling. However, to simulate the convective flow in the atmosphere or in stars, high Rayleigh number Ra must be approached (for estimates of typical dimensions, see table 1). In laboratory experiment nowadays, Ra up to 10^{15} were approached by several laboratories, however, high Ra experiments disagree with each other in the dependence of heat transfer efficiency (expressed by Nusselt number Nu) on the Ra [1]. This problem is still open for more than two decades and with this discrepancy, when we want to extrapolate known data to simulate the behavior of heat transfer in nature, we can end with the error exceeding one order of magnitude which is not acceptable.

Table 1: Examples of convection systems with estimates of their Rayleigh number Ra, Prandtl number Pr and the typical vertical scales L [1].

	Ra	Pr	L
Processor cooling device	10^6	0.7	1-10 cm
Indoor ventilation	$10^8 - 10^{10}$	0.7	1-10 m
Deep oceanic convection	$10^{23} - 10^{27}$	7	1-4 km
Mantle convection	$10^7 - 10^9$	10^{23}	700 km
Solar convection zone	$10^{20} - 10^{24}$	$10^{-7} - 10^{-3}$	$2 \cdot 10^5$ km

This high error is due to power behavior and is schematically pictured in figure 1 but this error can be even higher. These power scaling laws are all theoretically derived for the Oberbeck-Boussinesq fluid where the fluid properties change so little on given temperature difference ΔT that they can be approximated as constant except the density responsible for the fluid flow. When Oberbeck-Boussinesq approximation is not kept, heat transfer efficiency can also be affected which results in a misleading transition to a different scaling law as was discussed in [2, 3, 4, 5].

Moreover, one and the most used way to approach high Rayleigh number Ra in the experiment is to utilize working fluid state in the vicinity of the critical point (for helium and SF_6) or gas-liquid line in a fluid phase diagram. But here, properties of the fluid differ significantly so the measurements in this area must go hand in hand with the analysis of the non-Oberbeck-Boussinesq effects. A deep understanding of non-Oberbeck-Boussinesq effects could give a possible explanation of the discrepancies between experiments enduring for more than twenty years or at least it can be a piece of a big puzzle of effects occurring in the Rayleigh-Bénard convection. This is also the motivation of this study, evaluation of the non-Oberbeck-Boussinesq effects occurring in our experiments covering the range $10^8 < Ra < 10^{12}$.

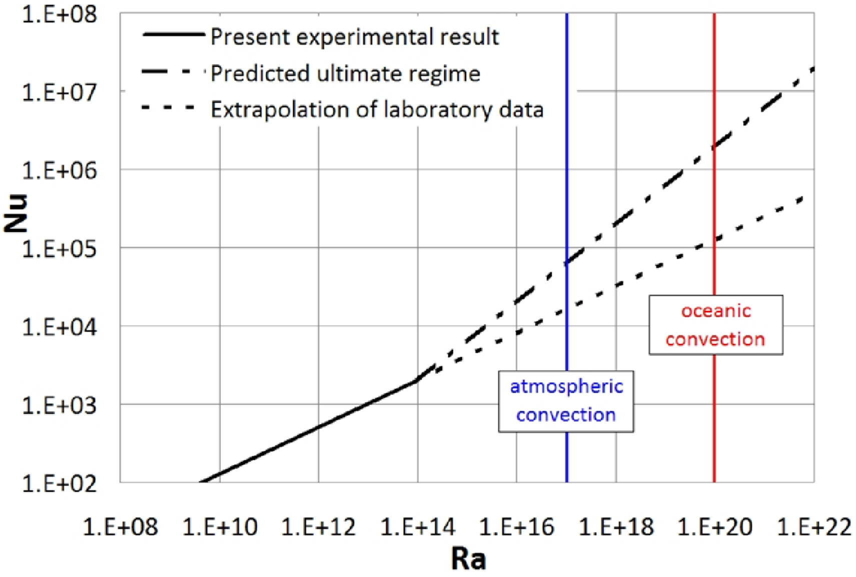

Figure 1: Demonstration of possible difference between heat transfer efficiency when trying to extrapolate measured data to extremely high Ra numbres.

Furthermore, the plentifully studied topic of RBC is the issue of boundary conditions. In the laboratory, it is impossible to realize infinite spatial dimensions in the horizontal direction, perfectly conducting plates, adiabatic walls, and other theoretically approachable properties. However, a detailed study of these boundary conditions can guide us to the application of mathematical corrections when the technical modification is not possible and it can lead to an agreement between the experiments as was in the case of side-wall corrections developed by Roche in [6] and applied on different cryogenic $Nu(Ra)$ data in [3].

Next, thermal boundary conditions at the bottom and top plates could also have an influence on the heat transfer efficiency. Two of these boundary conditions are pictured in figure 2 [7]. The effect on the heat transfer efficiency was studied numerically in [8] with an effect on Nu up to 30 % but later, recalculation made with higher precision in [9] resulted in no or negligible difference between regimes with the constant temperature and constant heat flux. Also in [10], the authors reported no difference in heat transfer efficiency between these two boundary conditions. However, the lack of experimental confirmation by different laboratories motivated us for this work. Huang et. al presented in [11] an experimental study of two boundary conditions pictured in figure 2, but they were mostly focused on the internal dynamics of the large scale circulation and not on the heat transfer efficiency. We present here the experimental study of the effects of two different thermal boundary conditions on the bottom plate in the range $10^8 < Ra < 10^{12}$ also together with evaluation of Reynolds number Re from the autocorrelation functions of the temperature fluctuations of the bottom plate.

My thesis is composed of five themed chapters. The first chapter is focused on the theoretical background of the Rayleigh-Bénard convection containing the definition of dimensionless parameters describing Rayleigh-Bénard convection such as Rayleigh number Ra, Prandtl number Pr, Aspect ratio Γ, Nusselt number Nu and Reynolds number Re. Also, a big part is devoted to non-Oberbeck-Boussinesq effects, corrections of Nu, boundary conditions, and large-scale circulation. In the second chapter, the goals of the

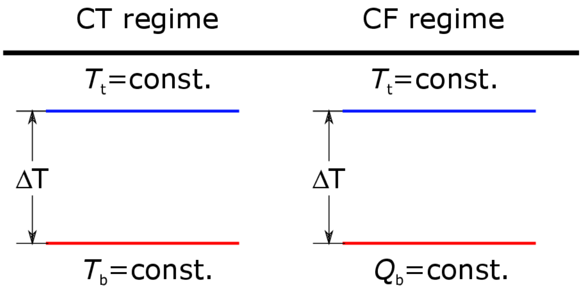

Figure 2: Basic scheme of two thermal boundary conditions. Adapted from [7]

thesis are stated and an introduction into the RBC with cryogenic helium is outlined. In the third chapter, the experimental apparatus is presented together with a brief description of the differences between the two data acquisition software programs used in this study. Also, a basic introduction into the PID regulation used for the stabilization of the temperature to satisfy the constant temperature boundary condition at the plates and experimental protocol is presented. The fourth chapter, presenting results, has three main parts. The first part contains the description of the working points and pictured fluid properties in the pressure range 1000–252000 Pa together with an evaluation of the non-Oberbeck-Boussinesq effects. Next, the comparison between constant temperature and constant heat flux boundary conditions is demonstrated firstly on the probability density functions of the temperature fluctuations, then on the standard deviation of the temperature fluctuations, and at last, their effect on the heat transfer efficiency. The third part presents the Reynolds number evaluation from the auto-correlation of the temperature signal from the bottom plate. In the last chapter, conclusions, and a summary of the results are provided.

1. Theory

1.1. Equations describing RBC

In order to describe Rayleigh-Bénard convection (RBC), one has to start with fundamental Navier-Stokes equation (1.1) together with continuity equation (1.2) and also Heat equation (1.3). These equations are

$$\rho \left(\frac{\partial \vec{u}}{\partial t} + \left(\vec{u} \cdot \vec{\nabla} \right) \vec{u} \right) = -\vec{\nabla} p + \mu \vec{\nabla}^2 \vec{u} + \rho \vec{g}, \tag{1.1}$$

$$\frac{\partial \rho}{\partial t} + \vec{\nabla} \cdot (\rho \vec{u}) = 0, \tag{1.2}$$

$$\frac{\partial T}{\partial t} + \vec{u} \cdot \nabla T = \kappa \vec{\nabla}^2 T. \tag{1.3}$$

Navier-Stokes equation describes the motion of Newtonian fluids and expresses the conservation of momentum. The continuity equation represents the conservation of mass and the Heat equation expresses the conservation of energy. Acting variables are ρ as the fluid density, $\vec{u}$ as the flow velocity, t is the time, p is the fluid pressure, μ is the dynamic viscosity, $\vec{g}$ is the gravitational acceleration of the size g which acts in direction of unit vector $\vec{k}$, κ is the thermal diffusivity and T is the temperature.

When the temperature difference ΔT between the top and bottom plate is small enough, fluid properties can be considered as constant except density ρ in the vertical direction in the buoyancy term $\rho \vec{g}$. In other words, only varying fluid property is density ρ responsible for the flow and depends linearly on the temperature

$$\rho(T) \approx \rho_0 \left(1 - \alpha \Delta T \right). \tag{1.4}$$

ρ_0 is the mean value of density at one typical position and α is the isobaric coefficient of expansion of the fluid. This is called Oberbeck-Boussinesq (OB) approximation. This approximation is usually supposed to be valid when condition $\alpha \Delta T < 0.2$ is kept. This condition means expansion of the fluid $< 20\%$, which approves approximation of incompressible fluid used in equations 1.1-1.3 [12].

1.2. Nondimensionalization

Even with OB approximation, the Navier-Stokes equation is difficult to numerically solve and for highly turbulent flows still impossible. Fortunately, dimensional analysis, when done correctly, can lead to another simplification of our three equations (1.1, 1.2, 1.3) and also show us the relative importance of fluid properties and parameters of the flow. Dimensional analysis ending with nondimensionalized equations also enables us to compare different experiments with different working fluids as a medium for convection.

How and when the nondimensionalization can be done is stated in Buckingham π theorem. It says that the equation with n independent physical variables expressed by k independent physical units will have after the process $n - k$ dimensionless parameters. Buckingham π theorem also serves as a method for nondimensionalization, however, this method doesn't lead to one specific solution but rather the method tells us how to generate these parameters. In this manner of countless possibilities of nondimensionalization, one must consider also the physical meaning of variables. Nondimensionalization, at its core, is not so hard and can be done just by some algebraic manipulations but this careless approach can lead to a complete disappearance of some term in a processed equation leaving some information lost [13].

In the case of this Master thesis, we will follow a scheme of the vast majority of studies oriented on RBC, and present here just a result of nondimensionalization of equations (1.1, 1.2, 1.3) under OB approximation [13]:

$$\frac{1}{Pr}\left(\frac{\partial \vec{u}}{\partial t} + \left(\vec{u}\cdot\vec{\nabla}\right)\vec{u}\right) = -\vec{\nabla}p + \vec{\nabla}^2\vec{u} + Ra\vec{k}T, \tag{1.5}$$

$$\vec{\nabla}\cdot\vec{u} = 0, \tag{1.6}$$

$$\frac{\partial T}{\partial t} + \vec{u}\cdot\nabla T = \vec{\nabla}^2 T. \tag{1.7}$$

In this set of equations, variables such as time, temperature, space coordinates are dimensionless but we kept the same notation to keep it neat. Two dimensionless parameters are Rayleigh number Ra and Prandtl number Pr:

$$Ra = \frac{g\Delta T L^3\alpha}{\nu\kappa}, \tag{1.8}$$

$$Pr = \frac{\nu}{\kappa}. \tag{1.9}$$

L is a distance between top and bottom plate and ν is kinematic viscosity defined as $\nu = \mu/\rho$.

Ra can be described as the ratio of buoyant force and the dampening effects due to viscosity and thermal diffusivity. For a system with infinite horizontal plates, the onset of convection occurs at $Ra_c = 1708$ [12]. For small $Ra > Ra_c$, the flow can also form some stable patterns and can be more easily described by numerical simulations but when Ra is getting bigger, the flow becomes more chaotic, turbulent, much harder to predict the behavior of the fluid, to simulate numerically and also experimentally.

Pr is an attribute of the working medium but it doesn't characterize the flow itself. For most of the gases, the value of the Prandtl number is close to 1.

1.3. Heat transfer efficiency

Heat transfer efficiency is expressed as how many times bigger is the heat flux through the cell in comparison with hypothetical heat flux without convection, just by heat diffusion, for given fluid properties and ΔT. This quantity describing the efficiency of heat transfer is called *Nusselt number*

$$Nu = \frac{q_b}{q_{cond}} = \frac{qL}{\lambda S\Delta T} \tag{1.10}$$

where q_b is measured heat flux and $q_{cond} = \lambda S \Delta T / L$ is diffusive heat flux for actual temperature difference ΔT with λ as heat conductivity, S is the area of the top or bottom plate and L is the distance between plates. Expression for q_{cond} is called *Fourier's law.*

When we look at an example of experimental dependence of Nusselt number Nu on Rayleigh number Ra in figure (1.1), we can see that for low Rayleigh numbers the Nusselt number is 1 meaning there is no convection and only heat transport is realized by conduction $q = q_{cond}$. The temperature profile is then linear as is schematically pictured in the upper part of figure 1.2. When Ra grows, the equilibrium is broken and the flow is starting to appear in the fluid. By convection, heat transport is much more efficient. In figure (1.1), you can see it could be by many orders of magnitude higher and grows with Rayleigh number. The temperature profile is also changed. Nearly whole temperature difference ΔT occurs at so-called thermal boundary layers in the vicinity of the top and bottom boundary while the warm and cold fluid in the bulk is effectively mixed by the convective flow resulting in approximately constant mean temperature (see figure 1.2 for the scheme of the flow and the temperature profile).

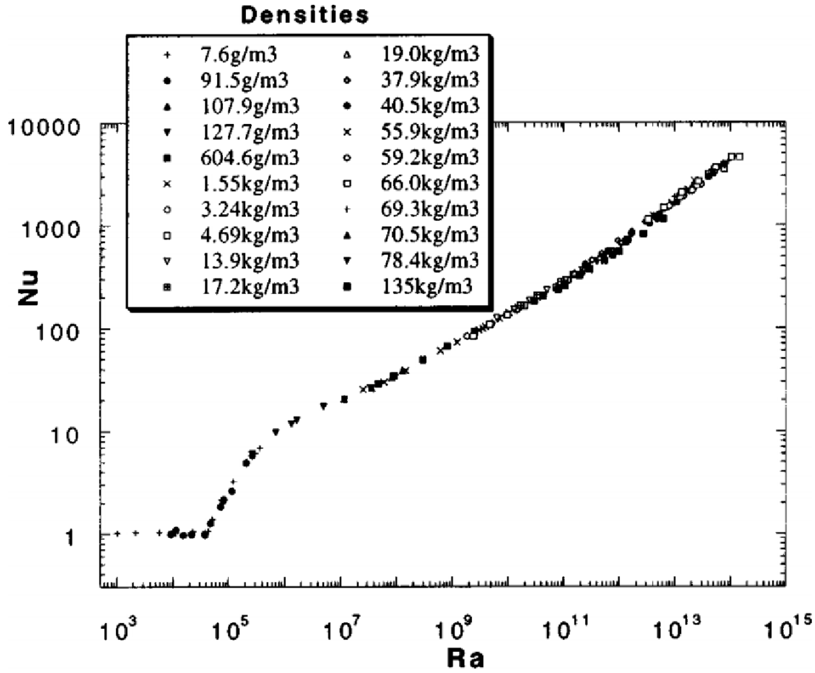

Figure 1.1: Experimental dependence of Nusselt number Nu on Ra measured with cryogenic helium gas. $Nu = 1$ means no convection, the temperature profile inside the experimental cell is linear as is displayed in figure 1.2. Then the efficiency of heat transfer is getting higher due to convective heat transfer. Figure taken from [14].

The thickness of the thermal boundary layers λ_{BL} is then given by this expression

$$\lambda_{BL} = \frac{L}{2Nu} \tag{1.11}$$

and the process of the heat transport through them is by diffusion. Overall heat transport is limited by these thermal boundary layers.

Dependence of Nu on Ra is usually presented as the scaling law

$$Nu \propto Ra^{\gamma} Pr^{\beta}. \tag{1.12}$$

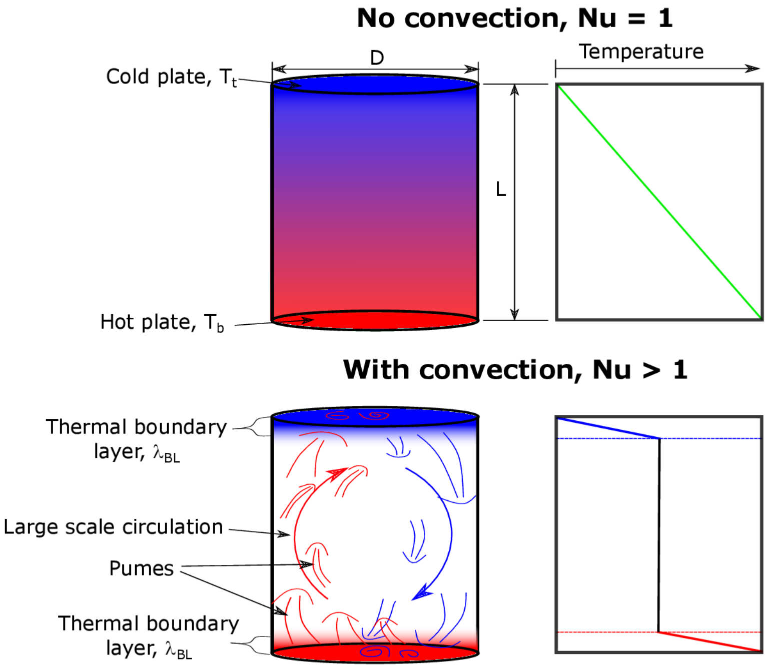

Figure 1.2: In the upper panel, the heat inside the cell is transferred just by conduction which is manifested in the linear temperature profile. The basic scheme of the Rayleigh-Bénard convection is in the lower panel. Whole temperature difference $\Delta T = T_b - T_t$ occurs on two thermal boundary layers of thickness λ_{BL} where the heat is transferred by conduction. In the bulk, the fluid is effectively mixed resulting in approximately constant temperature.

Dependence on the Prandtl number is relatively weak or none in our case of $Pr \approx 1$ [15] so afterward I will express this dependence just as $Nu \propto Ra^{\gamma}$.

One of the first scaling theories was based by Malkus after his own laboratory experiments. He derived scaling exponent $\gamma = 1/3$ from the fact that the ΔT occurs just on the thermal boundary layers and so heat transfer is limited by these boundary layers because in the convective turbulent core the temperature is effectively mixed and it doesn't limit the heat transfer efficiency. He also stated the fact that the heat transport is independent of the cell heigh L meaning the boundary layers don't communicate with each other.

Another scaling exponent, $\gamma = 2/7$, was presented by Shraiman and Siggia in [16] and by Castaing in [17]. Here they considered the assumption of the remaining thermal boundary layer in the viscous one.

The last presented scaling law is tied with the thickness of the thermal boundary layer. When it is getting smaller and smaller, there is a prediction of the disappearance of the thermal boundary layer or conversion from the laminar boundary layer into the turbulent one. This regime is called the *Kraichnan regime* or the *Ultimate regime* where the heat is transferred the most efficiently without limitation on the thermal boundary layers. This heat transport is also called *balistic heat transport*. This scaling is in the form $Nu \propto Ra^{\frac{1}{2}}$.

The Kraichnan regime is the most discussed because its existence was not confirmed by the scientific community [18]. It is supposed to be present in the convection within the stars, oceans, atmosphere. These high Rayleigh numbers occurring in nature are hard to reach in the laboratory and numerical experiment. Also, the reality demonstrates to us that many factors can affect the heat transfer and thus $Nu(Ra)$ dependence like the roughness of the surfaces inside the cell, geometrical properties, physical properties of the fluid and also the plates and side-walls, thermal boundary conditions and maybe many others [1, 18].

1.4. Boundary conditions

In theory, we suppose infinite horizontal perfectly conducting boundaries but this is never true. The first set of boundary conditions is given by the geometrical shape of the experimental cell. Mostly used is the cylindrical experimental cell schematically presented in figure 1.2. Geometrical proportions are characterized by a dimensionless parameter called *Aspect ratio* $\Gamma = D/L$ where D is the diameter and L is the height of the cell.

On all surfaces inside the experimental cell, the non-slip condition (velocity at walls and plates is zero) is expected to be true [19]. For thermal boundary conditions at side-walls, we usually work with the adiabatic case. No heat transport through the side-wall is desired and must be minimized because it changes the dynamics of the system. To minimize this effect, the technical solutions in the construction of the experimental cell could be done like in the case of our apparatus described in section 3.1. Also, mathematical corrections of Nusselt number derived by P. Roche in [6] when applied to previous experimental data with cryogenic helium in laboratories in Grenoble, Trieste, and Brno resulted in a collapse of all $Nu(Ra)$ dependences for Rayleigh numbers Ra in the range 10^7–10^{11} into one single dependence presented in [3]. However, side-wall correction doesn't explain discrepancy between experiments for $Ra > 10^{11}$.

In the experiment, thermal boundary conditions on the plates can approach a constant heat flux and constant temperature. Ideal constant temperature boundary conditions can be fulfilled when the heat capacity of the plate c_pl and thermal conductivity of the plate λ_{pl} are infinite (Dirichlet boundary condition). On the other side, the limit of low conducting plates corresponds to constant heat flux (Neumann boundary condition) boundary condition [10]. Infinite conductivity and heat capacity, naturally, can't be achieved in the real-life experiment so we can talk just about some partial justification of constant temperature boundary condition characterized by statistical description. The effect of the thermal conductivity of plates λ_pl was studied in [20] resulting in the decrease of the Nu for the case with the plate of lower conductivity λ_pl. In our experiment, we will focus on two regimes, one with the constant temperature at both plates (T_t and T_b), schematically pictured in figure 2 under the label CT regime, and the second one under the label CF regime where constant heat flux q_b is supplied into the bottom plate and the top plate is kept at fixed temperature value T_t.

Effect of CT and CF boundary conditions on $Nu(Ra)$ dependence was done numerically in [21, 10] resulting in a negligible effect. The experimental study was done by Huang et al. [11] and they were focused on the flow dynamics, flow strength, and reversals of the large-scale circulation resulting in the more dynamic behavior for the CT regime. Effect on the $Nu(Ra)$ dependence wasn't discussed by them and is presented by us in section 4.2.

1.5. Non-Oberbeck-Boussinesq effects

The scaling theories presented in section 1.3 were derived for the Oberbeck-Boussinesq fluid. However, few experimental datasets presented as a transition to the Kraichnan regime appeared to be measured near the critical point and the liquid-vapor where the fluid properties change dramatically and Oberbeck-Boussinesq approximation can't be never fully satisfied in this area [2, 3, 4, 5]. Next to the strong heat transfer enhancement due to violation of the Oberbeck-Boussinesq approximation, an asymmetry between thermal boundary layers can be observed. This non-Oberbeck-Boussinesq effect is visualized in figure 1.3. In the Oberbeck-Boussinesq case, the temperature of the bulk T_c measured by a sensor in the middle of the cell equals the mean temperature $T_m = (T_b + T_t)/2$. On the other side, in the non-Oberbeck-Boussinesq case, the temperature of the bulk T_c is shifted so $T_m \neq T_c$. This temperature shift is realized by the asymmetry in temperature difference on the top thermal boundary layer Δ_t and temperature difference on the bottom thermal boundary layer Δ_b.

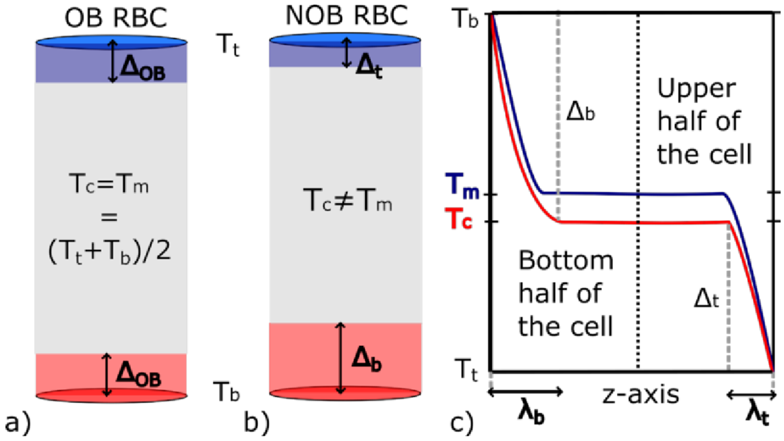

Figure 1.3: Scheme of the asymmetry in thermal boundary layers occurring in the RBC due to non-Oberbeck-Boussinesq effects. Δ_{OB} is the temperature difference at thermal boundary layers in the Oberbeck-Boussinesq case and Δ_t and Δ_b are temperature differences at top and bottom thermal boundary layer in the non-Oberbeck-Boussinesq case. Taken from [22].

The asymmetry of thermal boundary layers can be expressed by introducing X parameter

$$X = \frac{\Delta_t}{\Delta_b} = \frac{T_c - T_t}{T_b - T_c} \tag{1.13}$$

and when the temperature of the bulk T_c is not measured, the theoretical parameter X_{th} can be calculated as [18]

$$X_{th} = \left[\frac{\left(\frac{\alpha}{\nu\kappa}\right)_b}{\left(\frac{\alpha}{\nu\kappa}\right)_t} \left(\frac{\lambda_b}{\lambda_t}\right)^3 \right]^{1/4}, \tag{1.14}$$

where fluid properties with lower index b are calculated for the temperature of the bottom plate T_b and fluid properties with lower index t are calculated for the temperature of the top plate T_t. A clear correlation between X calculated from direct measurement, theoretically estimated X_{th} and the $Nu(Ra)$ dependence can be seen in figure 1.4. The asymmetry diverse for various experiments with various fluids as you see in figure 1.5 [4]. Analogous to X parameter, fluid properties can be used instead of temperature: $(FP_c - FP_t)/(FP_b - FP_c)$.

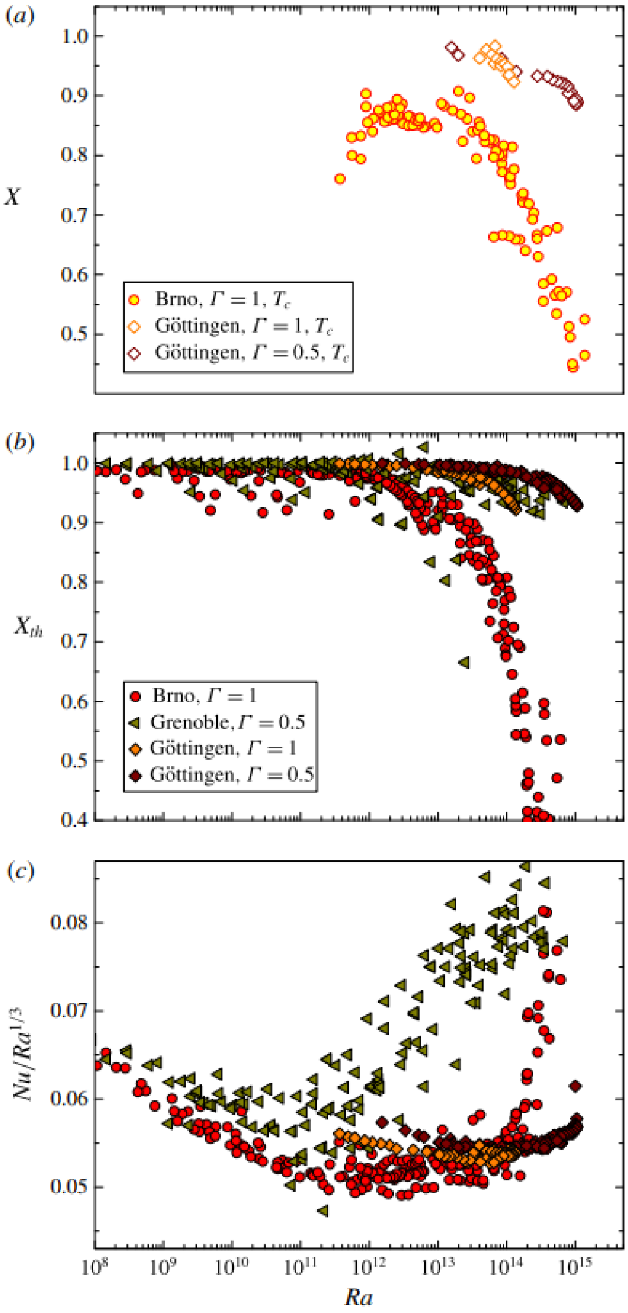

Figure 1.4: (a): Ra dependence of X parameter calculated from directly measured temperature of the bulk T_c on Ra. (b): Calculated theoretical parameter X_{th} from the fluid properties. (c): $Nu(Ra)$ dependence where there is clear correlation between decrease in X parameter and increase in Nu for Brno measurements. Taken from [18].

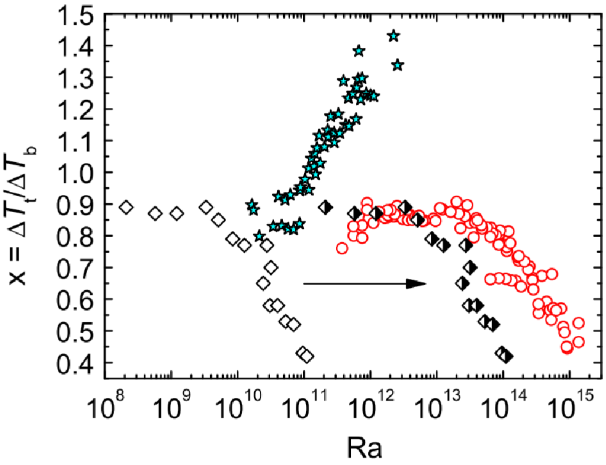

Figure 1.5: X parameter defined in 1.13 measured by different laboratories and for different working fluids where you can see X parameter rise for the water data (stars) and drop for He data (diamonds and circles). Half filled diamonds are corrected empty diamonds. Circles are data from Brno [4].

1.6. Large scale circulation dynamics

The flow inside the cell is organized into coherent structures, an interplay of plumes, and large-scale circulation (also called the wind) as is schematically displayed in figure 1.2. Thermal plumes are mushroom-shaped 2D structures of the surface area S and thickness comparable to the thermal boundary layer thickness λ_{BL} emitted from the vicinity of the plates. Such an amount of fluid of the heat capacity C_p and density ρ takes with it the heat $Q_p \approx S\lambda_{BL}C_p\rho\Delta T/2$ when is emitted from bellow or leaves behind the heat Q_p when is emitted from above. The same amount of heat must be delivered by the heater through the plate with thermal conductivity λ_{pl}. The heat through the fluid is transferred Nu times efficiently so the heat conductivity of the fluid can be considered as $Nu\lambda$. So to support the heat into the cell, the ratio $\lambda_{pl}/Nu\lambda$ must be high. Parameter with similar concept is $K = (\rho_{pl}C_{pl}\lambda_{pl})/(\rho C_p Nu\lambda)$ where also the ability to accumulate the heat is considered [23]. These ratios are calculated for our, Trieste and Grenoble experiment in table 4.1. Comparing parameters of plates among those experiments we can see that Brno values are the highest. We suppose that higher values mean a lower effect of plate properties on heat transfer and large-scale circulation in the cell.

In order to characterize the velocity field inside the cell, dimensionless parameter Reynolds number Re is used. In present high Ra experiments, using He or SF6 fluids, it is not possible to visualize the fluid movement. We can make it indirectly via a record of fluctuating temperature at selected points. There are several ways to determine the Reynolds number depending on the measurement method.

In one probe measurement, the definition of Reynolds number is

$$Re_{f0} = 2\frac{L^2}{\nu t_0} \tag{1.15}$$

where the specific turnover time t_0 is determined from the autocorrelation of the temperature fluctuation signal.

When two probe measurement is performed where we can assume no heat dissipation between them [24], Reynolds number can be calculated as

$$Re_p = \frac{Ld}{\nu \tau_p} \tag{1.16}$$

where d and τ_p stands for the distance between the probes and the time delay between the signals [25]. τ_p can be obtained from cross-correlations between the temperature fluctuations signal from the two probe measurements.

The last method is elliptic approximation designed for the general space-time cross-correlation function along with the homogeneous flow. More on the Reynolds number is in [25] and references therein.

In the experimental part, we will focus on Re_{f0} number, equation 1.15, evaluated from the temperature signal recorded inside the fluid and from the temperature of the plate. The aim is to see the interaction of the plate with the LSC in the experimental regimes CT and CF.

2. Goals of the Thesis

The aim is to perform experiments on heat transfer efficiency at a high intensity of turbulent convection (Rayleigh number Ra up to 10^{15}) using working points (temperature and pressure) in the phase diagram of cold helium gas (4He) close to the critical point (5.2 K, 227 kPa) and/or critical isochore. Finally, the influence of working point positions in the 4He phase diagram on heat transfer efficiency will be analyzed in detail. The experiment will take place at ISI Brno using the existing ConEV (Convection Experimental Vessel) experimental apparatus, specially designed for this purpose.

2.1. Helium as a working fluid

Cryogenic helium as a working fluid was used already in 1975 by Threlfall [26]. Due to a strong dependence of helium properties on temperature T and pressure p at cryogenic temperatures, it was possible to approach the value Ra 10^{17}, the highest obtained Rayleigh number in laboratory conditions (Oregon/Eugene, $\Gamma = 0.5$) [27]. The next advantage arising from the strong temperature T and pressure p dependence as well is an attainable high Ra range of more than 7 orders of magnitude with *in situ* tuning. Advantages arising from the cryogenic temperatures are good thermal isolation originating in a high cryogenic vacuum ($p \sim 10^{-6}$), radiation shields anchored at the helium bath resulting in no or negligible parasitic heat flux from the environment, the properties of the construction materials (for example high conductivity of copper) are better than those used at room temperature.

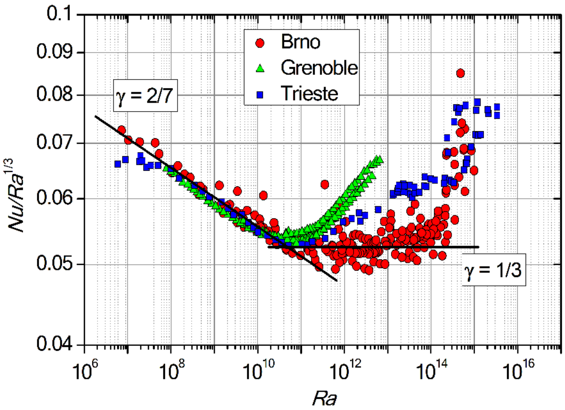

Figure 2.1: Experimental dependence of reduced Nusselt number Nu on Rayleigh number Ra in experimental cell of aspect ratio $\Gamma = 1$ from three different laboratories. Data are side-walls corrected. Up to $Ra \approx 10^{11}$, they all follow scaling $\gamma = 2/7$. For $Ra > 10^{11}$, they all start to disagree mutually. Taken from [28].

When we look at an experimental $Nu(Ra)$ dependence in figure 2.1 measured with cryogenic helium by three different laboratories (Brno, Trieste, Grenoble) in cylindrical cells of aspect ratio $\Gamma = 1$, we can see in the range of Rayleigh numbers $10^7 < Ra < 10^{11}$ nice mutual agreement in the $\gamma = 2/7$ scaling [3]. However, for higher Ra, the difference in scaling behavior is visible. Brno data follows the scaling $\gamma = 1/3$, in Grenoble $\gamma = 1/2$ and in Trieste, γ is something between [1, 4]. The transition into the 1/2 scaling (Grenoble) was presented as the transition into the Kraichnan regime [29].

The arguments against the transition to the Kraichnan regime were the effects of not satisfied Oberbeck-Boussinesq approximation, so-called non-Oberbeck-Boussinesq (NOB) effects, in the vicinity of the liquid-vapor line, critical point and the critical isochore in the phase diagram of the working fluid (see figure 2.2 for the position of Grenoble, Trieste and Brno data in the phase diagram). Near the critical point, fluid properties change significantly resulting in the possibility to reach very high Rayleigh numbers. However, this area must be treated really carefully because the aforementioned NOB effects can also lead to a dramatic increase in the heat transfer which can be incorrectly interpreted as the transition to the Kraichnan regime. Such a big enhancement due to NOB effects was presented in [4].

This still open and not fully understood topic was the motivation of this study, to repeat the measurements in the vicinity of the critical point and the critical isochore, but unfortunately, due to small leakage on the filling tube, we limited our measurements to pressures up to 130 kPa and thus not reaching the vicinity of the critical point and critical isochore. However, we still make it to measure Rayleigh numbers up to $6.32 \cdot 10^{12}$ so the problematic part $Ra > 10^{11}$ is still partly covered.

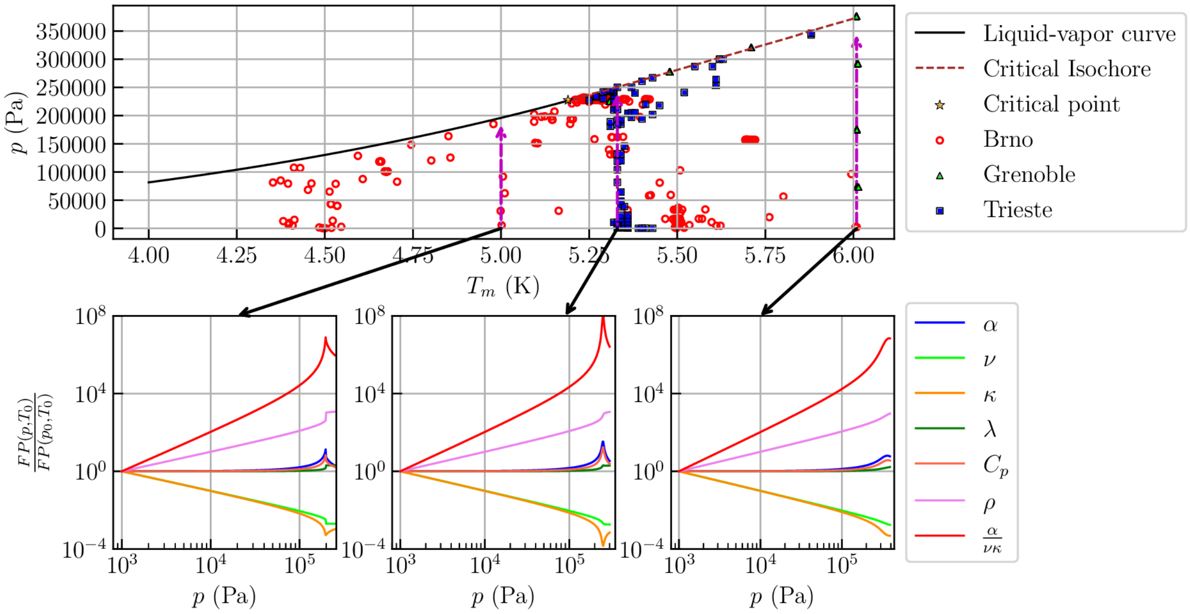

Figure 2.2: In the upper panel, phase diagram of helium with Grenoble and Trieste data is displayed. In the lower panel, relative fluid properties along the red arrows are evaluated. $p_0 = 1000\,\mathrm{Pa}$ and T_0 is 5.010, 5.330 and 6.009 K for respectively.

The measurement strategy in Grenoble and Trieste was, as you can see in figure 2.2 represented by red arrows, to keep the mean temperature T_m between the plates approximately the same and continue in the phase diagram upwards, so rising the pressure inside the cell. Trieste data were measured below the critical isochore near the critical point and Grenoble data were measured below the critical isochore. We decided to follow their strategy but with a lower mean temperature T_m to map the area below the liquid-vapor curve. You can also see calculated relative properties of the helium in the lower part of figure 2.2. They were evaluated by the relation $FP(p, T_0)/FP(p_0, T_0)$ where $p_0 = 1000\,\mathrm{Pa}$ and T_0 was 5.010 (Brno), 5.330 (Trieste) and 6.009 K (Grenoble).

3. Experimental set-up

3.1. Helium cryostat and convection cell

A helium cryostat with the cylindrical experimental cell was designed in the Institute of Scientific Instruments of the Czech Academy of Science in Brno [30].

Whole cryostat is pictured in figure 3.1. The cylindrical cell of hight $L = 0.3\,\mathrm{m}$ is confined by two oxygen-free high conductivity copper plates ($\lambda_p l = 2kWm^{-1}K^{-1}$ at $4.2\,\mathrm{K}$) of diameter $D = 0.3\,\mathrm{m}$, and thin ($0.5\,\mathrm{mm}$) stainless steel side-walls so the aspect ratio of our cell is $\Gamma = 1$. A central part of the convection cell can be exchanged to adjust Γ up to a value 2.5. The special connection between copper plates and side-walls (see figure 3.2) was used to minimize the side-wall effects discussed in section 1.4. Stainless steel has a low thermal conductivity so it also helps with reducing any undesirable heat transfer through the side-wall.

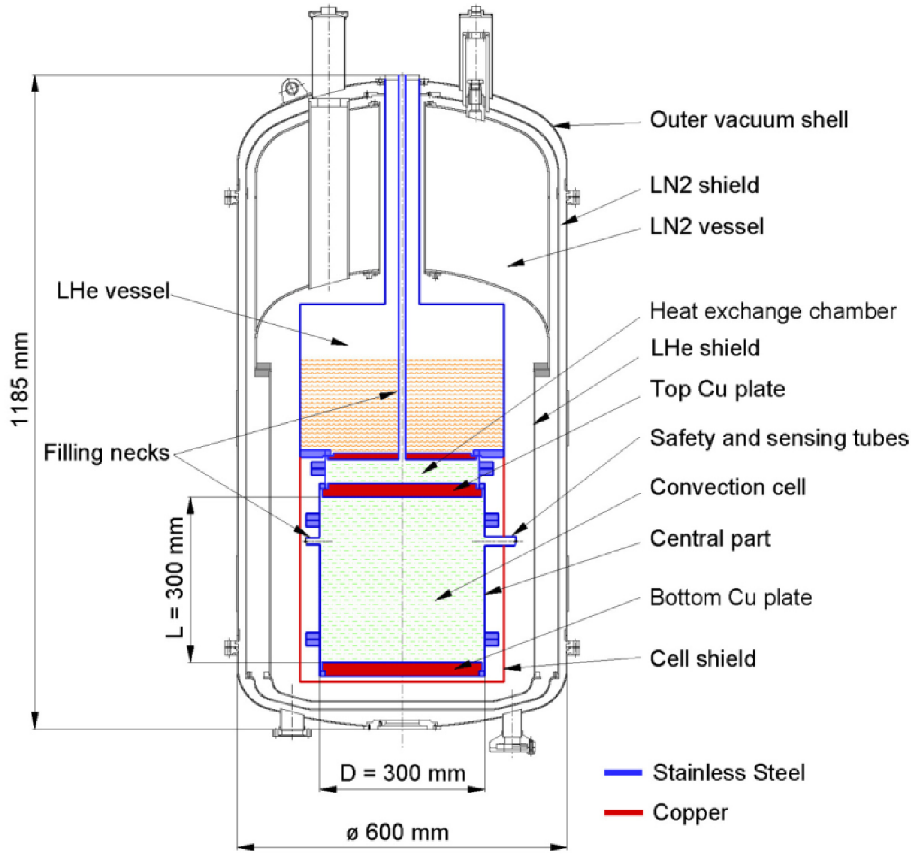
Outer vacuum shell
LN2 shield
LN2 vessel
LHe vessel
Heat exchange chamber
LHe shield
Top Cu plate
Safety and sensing tubes
Filling necks
Convection cell
Central part
Bottom Cu plate
Cell shield
1185 mm
L = 300 mm
D = 300 mm
ø 600 mm
Stainless Steel
Copper

Figure 3.1: The helium cryostat with the cylindrical experimental cell used for our mesurements [30].

From the outer side of the copper plates, the resistance heaters are glued into the spiral groove (see figure 3.3). The top heater is powered with Q_t and is used for a PID stabilization of the top plate temperature T_t. The bottom heater supplies the heat into the cell with a rate Q_b and it is also used for the PID stabilization of the bottom plate temperature T_b.

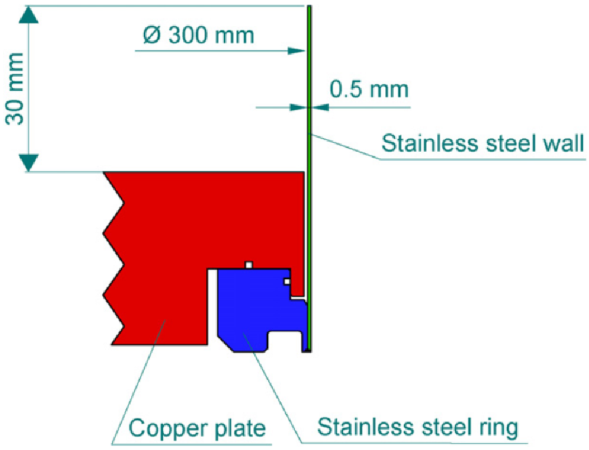

Figure 3.2: Special design of the connection between the copper plate and stainless steel side-wall of Brno cylindrical cell to minimize the heat transfer through the side-wall. Taken from [4].

The top plate is connected through the heat exchange chamber with a liquid helium (LHe) vessel (4.2 K) working as a heat sink for the heat transferred from the bottom plate into the top plate. The heat exchange chamber is filled with helium gas. One thermal shield (cell shield) surrounding the experimental cell is anchored to the bottom of the LHe vessel, one is anchored to a liquid nitrogen (LN_2) vessel (77 K) and next, an aluminum shield surrounding LN_2 vessel, that is cooled by cold gaseous nitrogen. On the bottom of the cell shield, cryosorbents are placed to improve the vacuum and so the isolation of the whole system.

3.2. Temperature sensors in the convection cell

The distribution of the temperature sensors in the convection cell is in figure 3.3. In sum, we use 12 temperature sensors in the middle of the cell and 3 sensors in each plate. These sensors are used to characterize the convection in the experimental cell.

The first type of temperature sensor is a small Ge-on-GaAs film resistance thermometer in the shape of $250\,\mu$ cube (type TTR-G in [31]). Their typical resistance is around $6\,\mathrm{k}\Omega$ and sensitivity $\simeq 1\,\mathrm{k}\Omega/\mathrm{K}$ in our measured range at 5 K. They are placed in pairs in two parallel horizontal planes, one in the middle height of the cell, the second one slightly above, and their vertical planes are perpendicular to each other as is in figure 3.3. Three of them are calibrated to measure the temperature inside the cell T_c. The rest is used with the combination of Lock-In amplifiers (Stanford Research Systems SRS830) connected through the Wheatstone bridges to the sensors where the voltage across the bridge is measured. From these uncalibrated thermometers, we detect small fluctuations in the temperature.

Second type is Ge sensor Lake Shore GR-200A-1500-1.4B precisely calibrated by The Physikalisch-Technische Bundesanstalt (PTB), metrology intitute in Germany. They are embedded in the center and near the edge of both Cu plates. Their absolute accuracy is 2 mK. These are used to determine the mean temperature of the plates. In each plate, two of them are used. They are marked T_{b1}, T_{b2}, T_{t1}, T_{t1} in the figure 3.3.

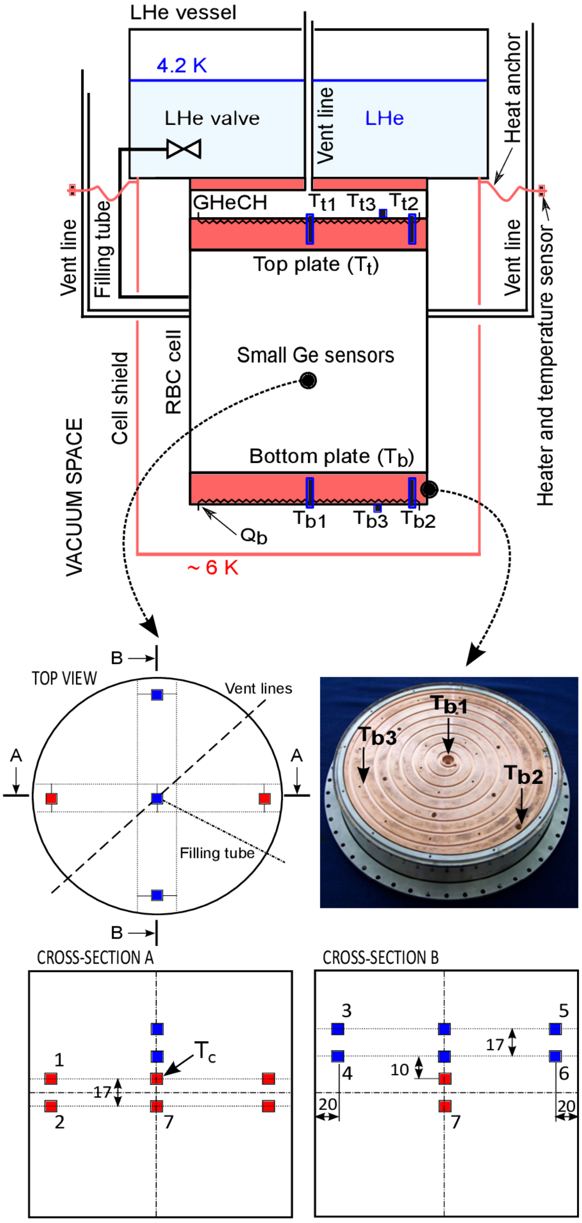
LHe vessel
4.2 K
LHe valve
Vent line
LHe
Heat anchor
GHeCH
T_{t1}
T_{t3}
T_{t2}
Top plate (T_t)
Vent line
Filling tube
Vent line
Heater and temperature sensor
Small Ge sensors
RBC cell
Cell shield
VACUUM SPACE
Bottom plate (T_b)
Q_b
T_{b1}
T_{b3}
T_{b2}
~ 6 K
B
TOP VIEW
Vent lines
A
A
Filling tube
B
Tb1
Tb3
Tb2
CROSS-SECTION A
1
T_c
17
2
7
CROSS-SECTION B
3
5
17
4
10
6
20
7
20

Figure 3.3: Detailed scheme of the temperature sensors distribution in the Brno convection cell. [23]

The last type of sensor is fast DT-670 Silicon Diode by LakeShore company. Calibration was done against the Ge sensors.

3.3. Data measurement

Data collection was performed by two of our LabView softwares written by T. Králík: CoCoS (Convection Control System) and HeTWiCA (Helium Turbulent Wind Control and Acquisition)

CoCoS: Software for data collection of the quantities needed to evaluate Ra, Pr and Nu. The sampling rate is asynchronous with an approximate frequency 1 Hz. In this system, data from Ge sensors inside the plates T_{b1}, T_{b2}, T_{t1}, T_{t2} and bulk temperature T_c from calibrated Ge-on-GaAs are recorded by Lake Shore 340 Temperature Controller with ± 2 mK uncertainty. The voltage U_b and the electrical current I_b to the bottom heater are recorded with uncertainty 0.5 % by Agilent 34410A. The pressure inside the cell p was measure by Baratron 690A 53T RB gauge with an uncertainty of 0.08 %. The typical range of the file sizes is between 4-8 MB.

HeTWiCA: For collection of thermal fluctuation data. This Software was implemented with a sampling rate of 100 Hz, and simultaneous reading. HeTWiCA reads data from Ge-on-GaAs sensors and from the diodes inside the plates (T_{b3} and T_{t3}). The typical range of the file sizes from the HeTWiCA is between 120-200 MB.

3.4. PID regulation

Until now, build-in PID in the Lake Shore 340 Temperature Controller was used in the case of the top plate, and the heater in the bottom plate was powered by constant heat flux q_b. However, this LakeShore build-in PID was enough just for the long-term stabilization in the sense of the mean temperature. It was used to avoid any trend, meaning, it doesn't react to the fast temperature fluctuations but kept mean temperature and so ΔT in the cell. To minimize temperature fluctuations of plates caused by turbulent convection in the cell, a new PID stabilization system was designed by Tomáš Králík. The system is controlled by a new LabView software HeTWiCA also designed by Tomáš Králík.

The temperature from the chosen sensor goes to the PID as an input, is compared with the adjusted setpoint, deviation from the setpoint e is then used to calculate the output. This scheme is in figure 3.4. In our case, PID was connected to the heaters on the outer side of the plates and the output parameter is the voltage U and the electrical current I.

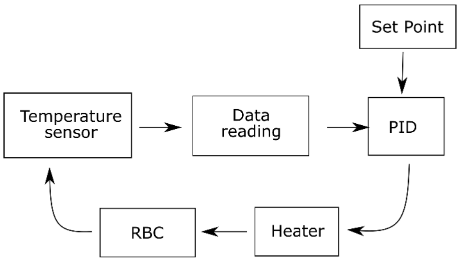

Figure 3.4: Basic scheme of the closed-loop PID regulation of our experiment.

Equation of the PID regulator is

$$output = P\left(e + \frac{1}{I}\int edt + D\frac{de}{dt}\right). \tag{3.1}$$

To tune PID parameters, we used a parameter estimation method called Internal Model Control (IMC) rules

$$P = \frac{\tau_p + 0.5\theta}{K_p\left(\tau_c + 0.5\theta\right)}, \quad I = \tau_p + 0.5\theta, \quad D = \frac{\tau_p\theta}{2\tau_p + \theta}, \tag{3.2}$$

where τ_p is the process time constant, K_p is the process gain, θ is the process dead time and τ_c is the parameter we can choose based on how aggressive we want PID to be (lower τ_c, higher aggressivity). $\tau_c = 0.1\tau_p$ is for the aggresive PID and $10\tau_p$ is for more slower but robust PID. τ_p, K_p, and θ are the characteristics of the system we want to regulate. To get them, we need to know the response of the system. In our case, it is a response of the temperature of the bottom plate T_b on the heater voltage U_b. This response was got by many step changes in the heater voltage U_b. Output bottom heater voltage U_b and the response of the temperature of the bottom plate T_{b3} from our step test are in figure 3.5.

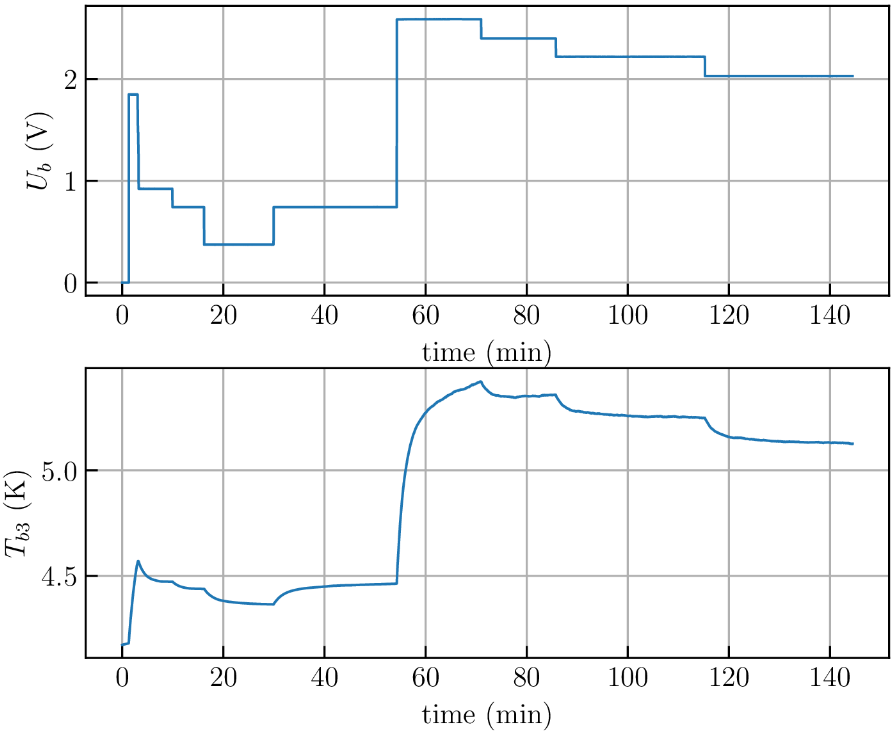

Figure 3.5: To get characteristic parameters K_p, τ_p and θ needed for the PID tuning, the step-test was performed. In the upper panel, the input voltage U_b into the bottom heater is recorded. In the lower panel, for every step change in the input voltage U_b, there is a corresponding temperature change of the bottom plate T_{b3} measured by fast Si diode.

Characteristic parameters K_p, τ_p, and θ are obtained from the mathematical fit of the temperature in the step test. Used function is

$$\begin{aligned} f(t < \theta) &= T_{b3}(t_0) \\ f(t \geq \theta) &= T_{b3}(t_0) + \left(1 - e^{\frac{t-\theta}{\tau_p}}\right) K_p \Delta U_b \end{aligned} \tag{3.3}$$

where ΔU_b is the size of the step made in the voltage signal.

IMC rules are just an estimation of the parameters so manual tuning is inevitable to get the best performance. An illustrative temperature signal where we tried to set different PID parameters is in figure 3.6. There you can also see bad tuning with a big overshot.

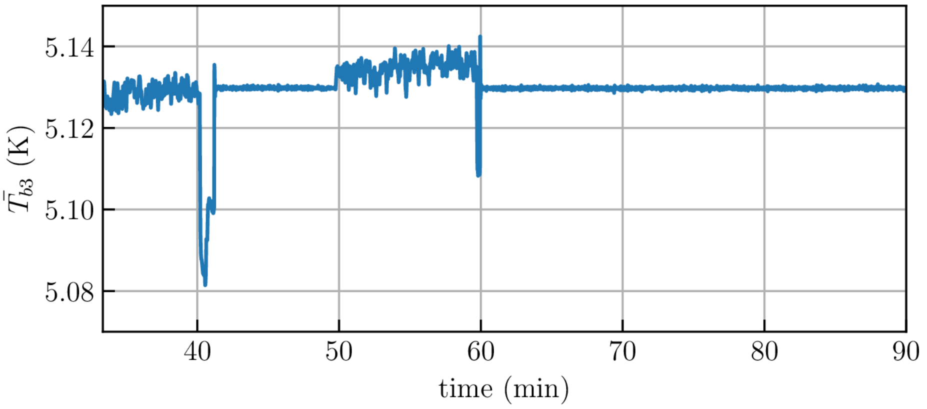

Figure 3.6: Illustrative figure of temperature signal for different PID parameters where also bad tuning can be seen.

In our case, we want to have fluctuations of the temperature as small as possible to approach constant temperature boundary conditions as much as we can.

The difference between temperature fluctuations of the bottom plate with (CT boundary condition) and without PID (CF boundary condition) is in figure 4.9 and is more discussed in the section 4.2. The top plate was still stabilized by slow LakeShore build-in PID regulation on the base of temperature T_{t1} in measurements presented in this study. The reason for this was caused by convection in the heat exchange chamber disturbing the diode measurement T_{t3}.

3.5. Experimental protocol

The experimental protocol is as follows.

- Filling the cell with a specific amount of helium
- Setting the temperature of the top plate T_t on the PID stabilization of the Lake Shore 340 Temperature Controller
- For CF regime: setting Q_b on the heater. For CT regime: setting T_b in the HeTWiCA software (section 3.3)
- Stabilization of temperatures of RBC and measurement
- For the known state of He (P, T_m), the fluid properties like α, ν, and κ are obtained from the HEPAK software [32]
- Ra, Pr, Nu evaluation and analysis of temperature signals

4. Results

Positions of experimental working points measured within this work (helium fluid states at mean temperature T_m and pressure p inside the cell) in the p-T phase diagram are in figure 4.1 where our working points are marked together with their corresponding ΔT. Relative fluid properties $FP_{rel}(p,T) = FP(p,T_0)/FP(p_0,T_0)$ are shown in figure 4.2. The base value they all relate to is our working point with lowest pressure $p_0 = 1038\,\mathrm{Pa}$ and mean temperature $T_0 = 5.010\,\mathrm{K}$. Also, we present a table 4.1 with characteristic properties for our, Trieste and Grenoble data.

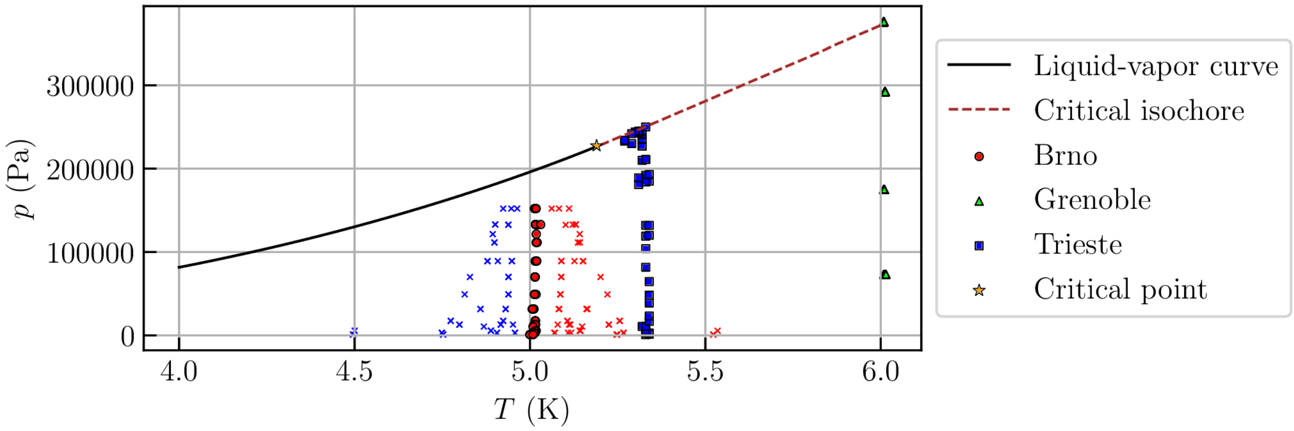

Figure 4.1: p-T phase diagram of the helium with marked helium states at T_m in our Brno measurements displayed by red circles together with temperatures of the top and bottom plate represented by crosses. Working points used in Grenoble and Trieste experiments are displayed as well.

Table 4.1: Experimental quantities relevant for generation of cryogenic turbulent RBC flows in the Brno experimental cell in comparison with Grenoble and Trieste cells. Adapted from [23]

	unit	Brno	Trieste	Grenoble	Brno	Trieste	Grenoble	Brno	Trieste	Grenoble
Ra	1	2.33E+08	3.45E+08	2.44E+08	1.34E+10	1.66E+10	1.30E+10	2.18E+12	2.16E+12	2.36E+12
Nu	1	41.7	43.7	39.0	138.3	138.3	128.7	717.8	746.1	821.2
Pr	1	0.68	0.68	0.77	0.71	0.70	0.97	1.00	0.97	2.51
T_m	K	5.009	5.33	6.009	5.016	5.34	6.009	5.009	5.33	6.009
ΔT	K	1.027	0.054	0.014	0.183	0.073	0.062	0.196	0.053	0.152
p	Pa	1032	2922	73190	17427	16790	175100	120666	132000	376200
ν	$\frac{\mathrm{m}^2}{\mathrm{s}}$	1.26E-05	5.00E-06	2.43E-07	7.40E-07	8.66E-07	9.56E-08	9.50E-08	9.96E-08	3.34E-08
κ	$\frac{\mathrm{m}^2}{\mathrm{s}}$	1.85E-05	7.33E-06	3.17E-07	1.04E-06	1.23E-06	9.87E-08	9.47E-08	1.03E-07	1.33E-08
α	1/K	2.00E-01	1.89E-01	2.04E-01	2.13E-01	1.98E-01	2.98E-01	3.79E-01	3.38E-01	1.04E+00
λ	$\frac{\mathrm{W}}{\mathrm{m\ K}}$	9.57E-03	1.01E-02	1.16E-02	9.65E-03	1.02E-02	1.25E-02	1.05E-02	1.11E-02	1.82E-02
ρ	$\frac{\mathrm{kg}}{\mathrm{m}^3}$	0.10	0.27	6.37	1.72	1.55	17.70	15.03	15.12	70.80
c	$\frac{\mathrm{J}}{\mathrm{kg\ K}}$	5203	5218	5742	5372	5339	7124	7367	7130	19370
$\alpha\Delta T$	1	2.1E-01	1.0E-02	2.8E-03	3.9E-02	1.4E-02	1.8E-02	7.4E-02	1.8E-02	1.6E-01
Q_b	W	0.095	0.009	0.001	0.056	0.041	0.009	0.344	0.173	0.203
$\frac{\lambda_{pl}}{Nu\lambda_f}$	1	5539.0	4514.4	2658.5	1655.8	1415.9	748.9	293.8	241.9	80.2
K	1	13796.1	4202.9	93.6	230.6	220.3	7.6	3.4	2.9	0.1

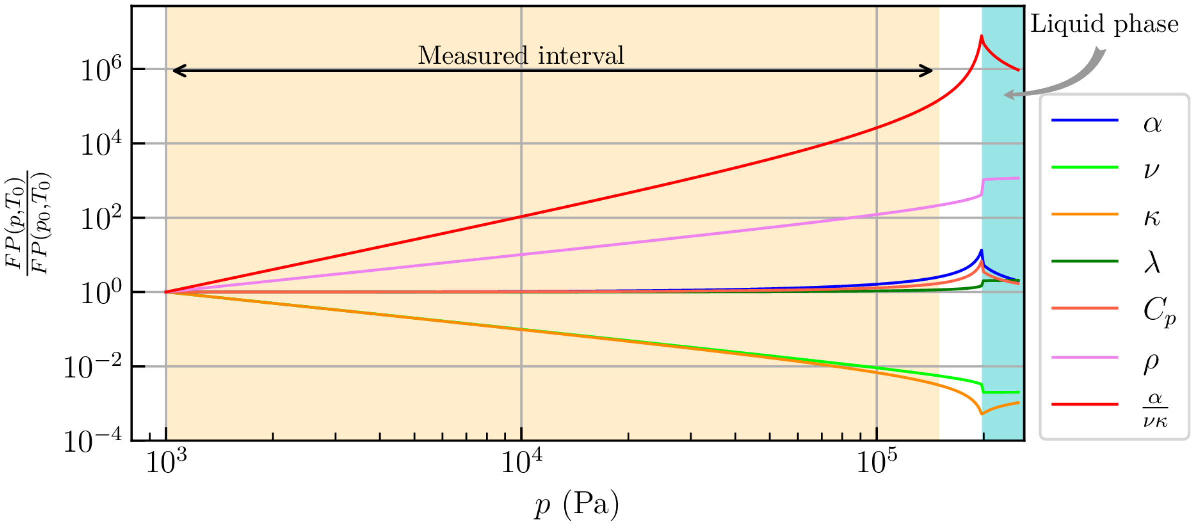

Figure 4.2: Relative fluid properties $FP_{rel}(p,T) = FP(p,T_0)/FP(p_0,T_0)$ where values $p_0 = 1038\,\mathrm{Pa}$ and $T_0 = 5.010\,\mathrm{K}$ are used which are the parameters of the measurement with lowest Ra. You can see a difference of 5 orders of magnitude for the ratio $\alpha/\nu\kappa$ which corresponds to the difference between the lowest measured Ra 10^8 and the highest Ra 10^{12}. Also the transition to the liquid phase is displayed to show, how close we got to the liquid-vapor line.

4.1. Evaluation of non-Oberbeck-Boussinesq effects

As was presented in [4], using mean temperature $T_m = (T_b + T_t)/2$ for evaluation of Nu and Ra can lead to spurious conclusions about $Nu(Ra)$ dependence. It is due to the asymmetry in thermal boundary layers resulting in a shift of the bulk temperature T_c so $T_m \neq T_c$. For this reason, it is convenient and suggested to directly measure temperature T_c of the bulk. The asymmetry between the boundary layers is expressed by X parameter (equation 1.13) in figure 4.3. The value 1 means the ideal Oberbeck-Boussinesq (OB) case. A decreasing trend of X with increasing Ra is obvious but in comparison with figure 1.4, the drop of our X parameter is small. The temperature difference occurring on the top boundary layer Δ_t is getting smaller compared with the temperature difference occurring on the bottom boundary layer Δ_b which is in agreement with [18].

However, in the condition $\alpha\Delta T$ serving as the OB criterion, when displayed for our experiment (see fig. 4.4), there is no systematic increase. For most of our measurements, $\alpha\Delta T$ is kept under the value 0.1 and even under 0.05 where we can consider our working fluid with the Oberbeck-Boussinesq approximation with certainty. You can see that for three measurements, the value of $\alpha\Delta T$ exceeds the limit value 0.2 so the criterion of OB approximation in these measurements can't be satisfied there. This departure from the OB approximation also can be seen in figure 4.5 where the asymmetry of the boundary layers is expressed by the properties of the fluid α, ν, κ, λ and ratio $\alpha/\nu\kappa$. In figure 4.5, like in figure 4.3, the value 1 means the ideal OB case. These values, where $\alpha\Delta T > 0.2$, are not visible on the behavior of the X parameter in figure 4.3.

How fluid properties change within given ΔT for approximately similar $Ra \approx 7.1 \cdot 10^9$ is presented in the figure 4.6. The case, when the $\alpha\Delta T > 0.2$ measured at $p = 10535\,\mathrm{Pa}$,

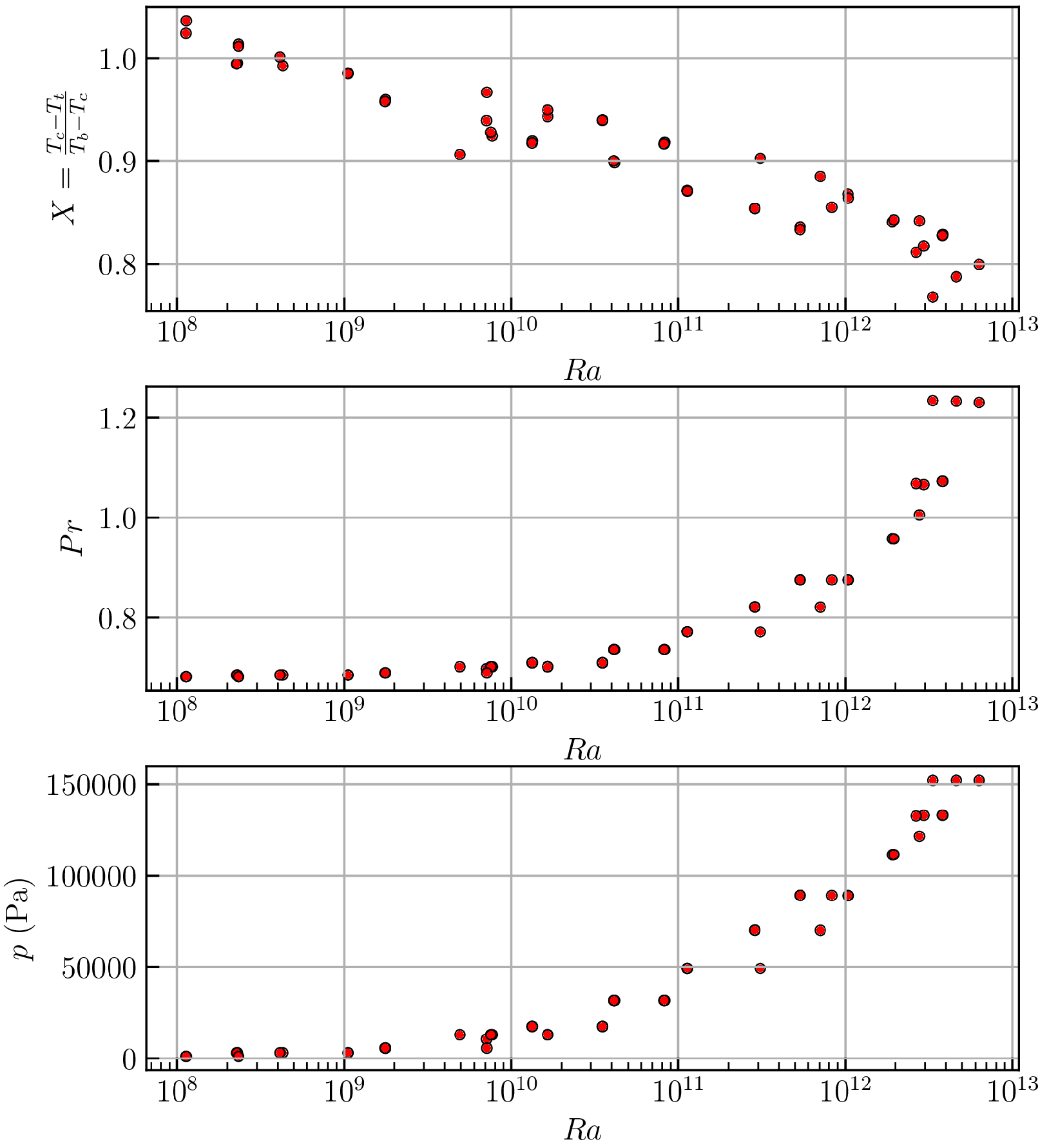

Figure 4.3: Top panel: X parameter defined in 1.13 and also presented in figure 1.5 measured in our Brno experiment. Middle panel: Prandtl numbers Pr evaluated for every measurement. Bottom panel: Pressure p inside the experimental cell.

is on the left panel and on the right panel $\alpha\Delta T = 0.058$ measure at $p = 5618\,\text{Pa}$. A clear difference is visible.

When we take a look on the meassured $Nu(Ra)$ dependence in figure 4.7 where we displayed $Nu(Ra)$ dependences calculated from the temperature of the bottom plate T_b, top plate T_t, mean temperature T_m, and the bulk temperature T_c. There is no big enhancement of the Nusselt number Nu but for $Ra > 10^{11}$, the values of $Nu/Ra^{1/3}$ start to diverge more pronouncedly. But the difference between using T_m and T_c remains small and the steeper $Nu(Ra)$ dependence at high Ra ($Ra > 10^{12}$ in our case), deviates from $\gamma = 1/3$ exponent toward higher value even for both T_m and T_c. Thus the divergence observed in experiments in figure 2.1 and 4.8 cannot be simply explained by using temperature T_c of bulk fluid in $Nu(Ra)$ evaluation. However, there is a growing difference

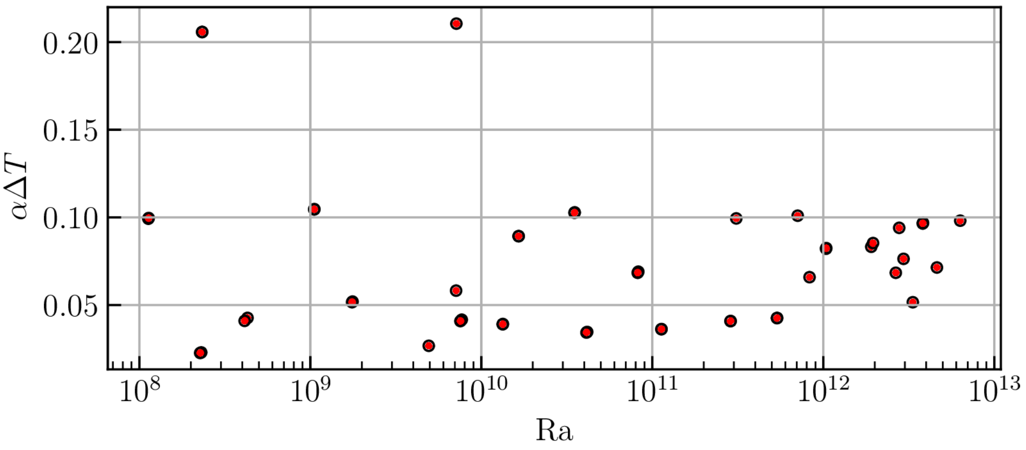

Figure 4.4: Criterion for the Oberbeck-Boussinesq approximation $\alpha\Delta T < 0.2$ is not satisfied for three of our Brno measurements.

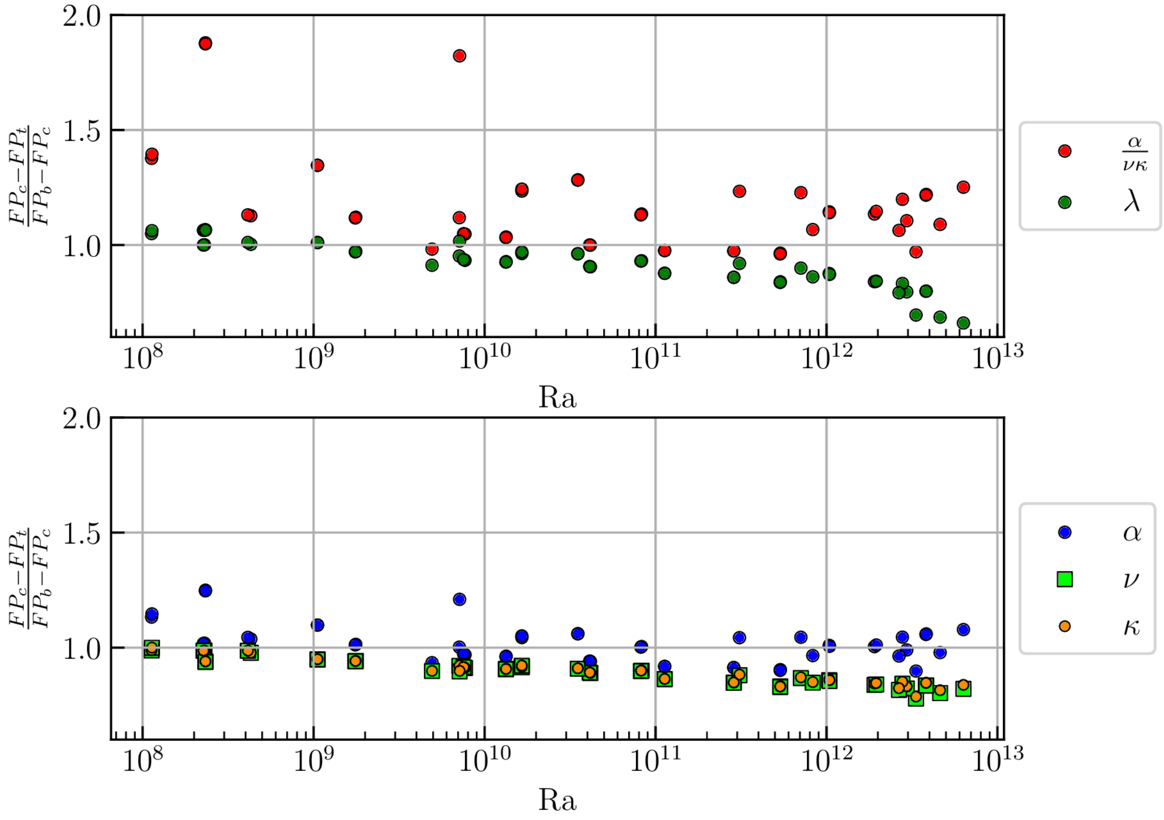

Figure 4.5: Behavior of the $\alpha\Delta T$ can be clearly seen in the behavior of the ratio $\alpha/\nu\kappa$, just with the reversed sign. Other properties are nearly one meaning the most Oberbeck-Boussinesq case. Thermal conductivity of the fluid λ follows a rise for $Ra > 10^{12}$.

between using T_b and T_t. This a consequence of the non-Oberbeck-Boussinesq effects, particularly high variability of the fluid properties inside the cell. Next to this systematic growing divergence in Nu, there is also a shift in Rayleigh number Ra pictured by black

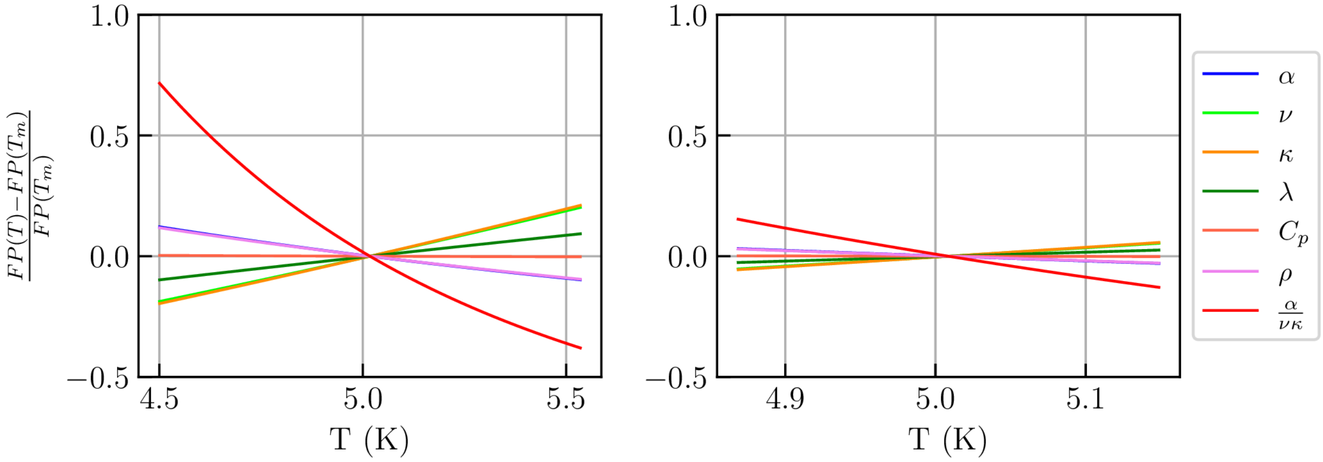

Figure 4.6: Change of relative fluid properties on given ΔT in the cell at $Ra \approx 7.1 \cdot 10^9$. Base value was chosen the mean temperature T_m.

lines connecting the corresponding values calculated for one measurement also due to high variability of the fluid properties inside the cell.

The results presented in this section were not affected by different thermal boundary condition on the bottom plate (CT and CF regime).

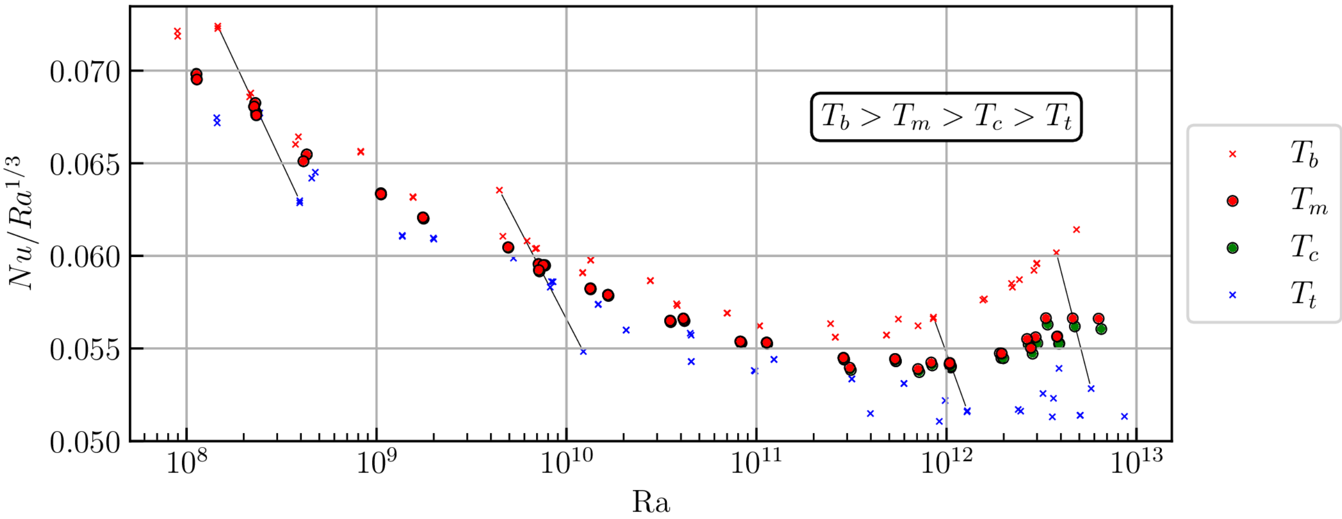

Figure 4.7: Reduced Nusselt number Nu on Rayleigh number Ra for our Brno measurements where all fluid properties are calculated from temeperature of the bottom plate T_b, top plate T_t, mean temperature T_m and bulk temperature T_c. Connecting black lines are for better orientation in the graph because non-Oberbeck-Boussinesq effects cause the shift in Nu and also in Ra and thus mixing the points.

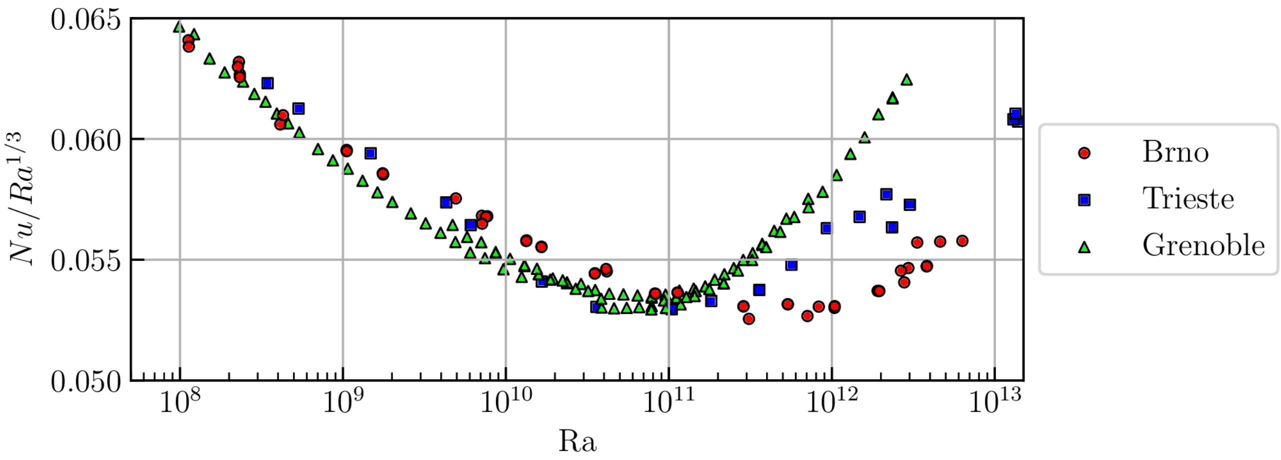

Figure 4.8: Reduced Nusselt number Nu on Rayleigh number Ra for our new Brno data (previous data are in figure 2.1) in comparison with data from Grenoble [29] measured just around $T_m \approx 6.009\,\mathrm{K}$ and from Trieste [33] measured around $T_m \approx 5.330\,\mathrm{K}$ laboratories where they also use a cell with aspect ratio $\Gamma \approx 1$ and cryogenic helium as a working fluid (for position in the p-T phase diagram, see figure 4.1). All Nu data are side-walls corrected.

4.2. Effect of thermal boundary conditions

In figure 4.9, there is a signal of the temperature fluctuations δT of the bottom plate reduced by ΔT for the case with PID (CT boundary condition) and without PID (CF boundary condition) and also with their corresponding probability density functions (PDF). You can see a significant narrowing of the PDF for the case with PID turned on. (CT)

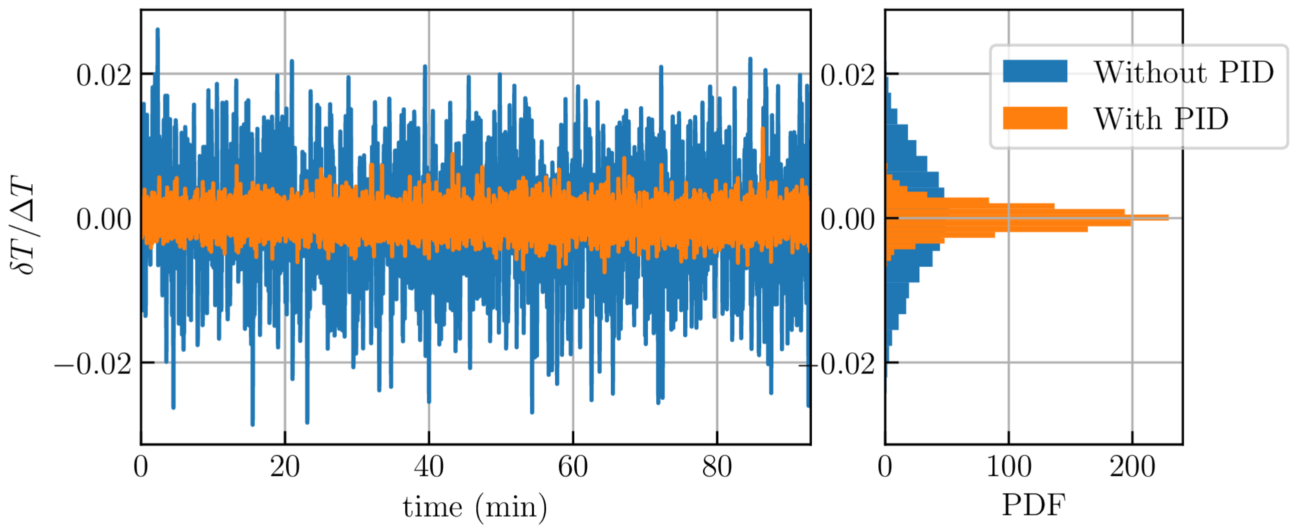

Figure 4.9: Record of the temperature fluctuations measured on the bottom plate with (CT regime) and without PID (CF regime). Also their corresponding probability density functions are displayed. Clear narrowing is visible.

PDFs of the temperature fluctuations $\delta T/\Delta T$ of the top and bottom plate from all our measured working points for both, CT and CF cases, are presented in figure 4.10.

There you can see some PDF narrowing on the bottom plate dependent on the Rayleigh number Ra for the case with constant heat flux. However, the PDFs for the CT boundary condition where the PID is on are nearly the same width for all measured Ra. This result can be assumed as feedback that our PID implementation works well for both high and relatively low Rayleigh numbers and so we can consider our constant temperature boundary condition as stable.

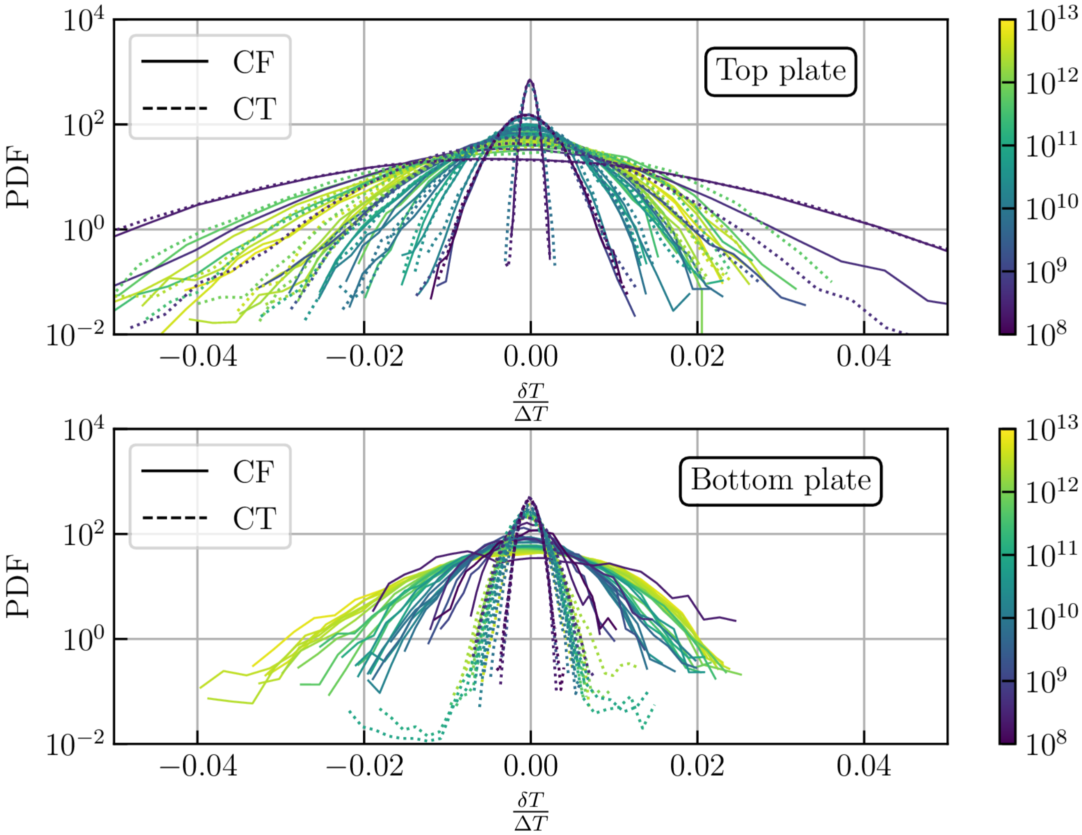

Figure 4.10: Calculated probability density functions for all our measurements. For the bottom plate case, a clear distinction between CF and CT regime is visible. In the CF regime, the range of the temperature fluctuations is growing with rising Ra. The same trend can be seen for the CT regime but the dependence is much weaker. In contrast, the top plate probability density functions for the CT regime are mixed with the CF regime.

But when we look at PDFs of the temperature fluctuations on the top plate in figure 4.10, all of them (CT and CF) are mixed up with no possible distinction between these two regimes. This can be interpreted as the fact, that the bottom boundary condition has no clear effect on the top boundary conditions.

Another effect of the CT condition can be displayed by the normalized standard deviation of temperature σT as on the figure 4.11. In this form and also for the PDFs, Huang et al. in [11] also justified their constant temperature boundary condition. But in their case, they had a decrease with increasing Ra whereas we have there an opposite trend.

In figure 4.11, we can see a clear distinction for CT and CF boundary conditions for the $\sigma T_b/\Delta T$ of the bottom plate but in the case of the top plate, there is no evidence of the influence on the $\sigma T_t/\Delta T$ of the fluctuations of the top plate by changing thermal boundary condition on the bottom plate between CF and CT in the whole studied range

$10^8 < Ra < 10^{12}$. However, we do not exclude the possibility of the change of dynamical properties such as the direction change of the large scale flow as is described in the [11]. A brief analysis of the large-scale flow reversals is in the Letter [23] which is now under review and also is in the appendix of this diploma thesis. A more detailed study of the dynamical properties is planned to publish later.

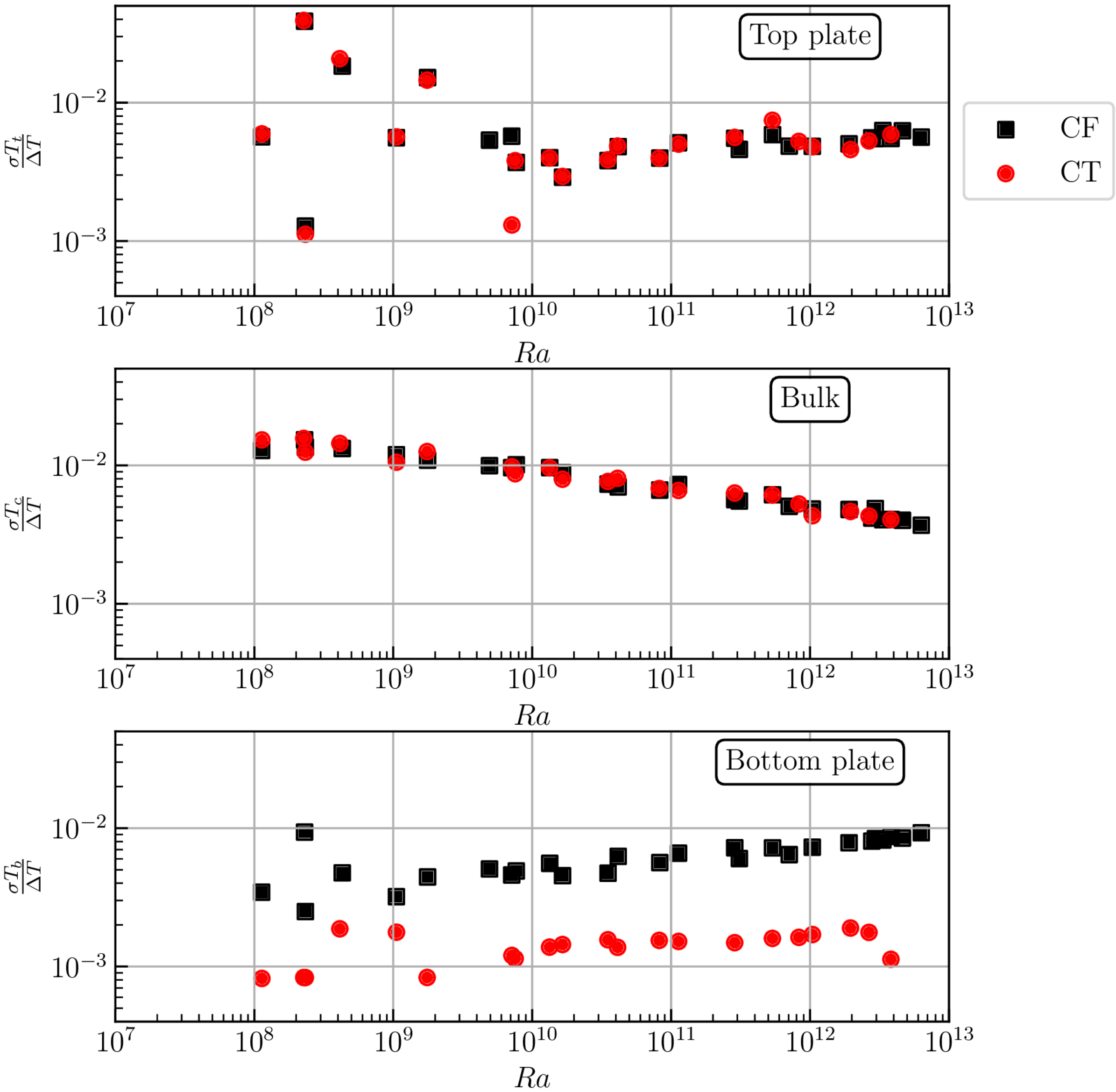

Figure 4.11: Calculated normalized standard deviations of the temperature fluctuations of the bottom plate, top plate and also temperature fluctuations of the bulk T_c. The increasing trend with increasing Ra for the bottom plate is obvious. A clear decrease is visible for the temperature fluctuations in the bulk with growing Ra.

And finally, the effect of these boundary conditions on the $Nu(Ra)$ dependence. In figure 4.12, there you can see no or negligible difference between CT and CF regimes. More details on this topic are in the appendix of this thesis.

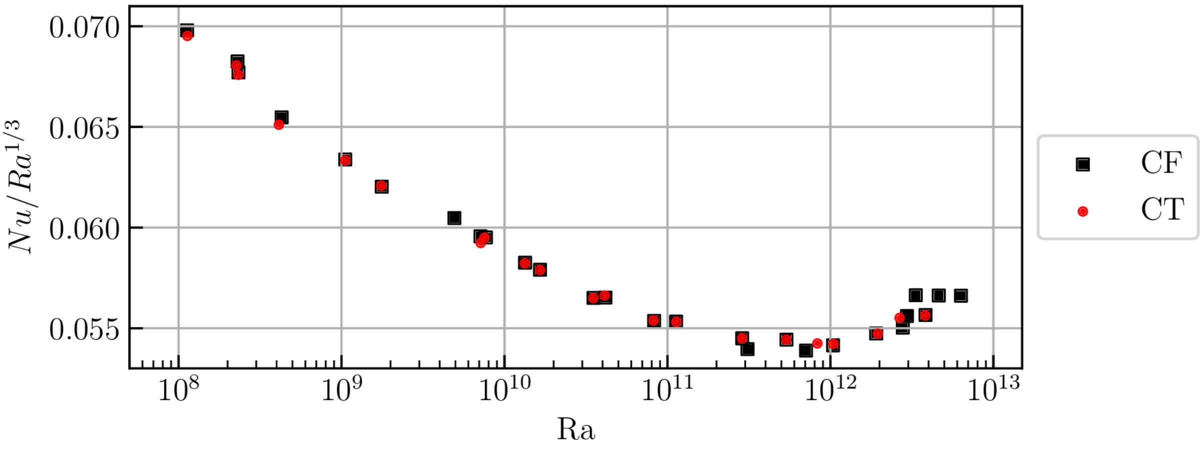

Figure 4.12: A comparison between reduced Nu on Ra for CT and CF regimes.

4.3. Large scale flow

The period of large-scale circulation t_0 is usually analyzed from the sensors placed in the bulk. Here we present that it is possible to evaluate the period t_0 also from the auto-correlation functions based on the data from the temperature sensor T_{b3} placed on the outer side of the bottom plate.

The characteristic time of the large-scale circulation t_0 needed for the calculation of Reynolds number Re_{f0} defined by equation 1.15, is evaluated from the position of the first peak in the calculated auto-correlation functions of the temperature signal. We used for the evaluation signal from fast Si diode T_{b3} (see figure 3.3).

Auto-correlation function of the temperature signal at $Ra = 1.9 \cdot 10^{12}$ for the CF boundary condition is in figure 4.13 and for the CT at the bottom plate in figure 4.14. There can be seen a big difference between these two auto-correlation functions. For the CT boundary condition, the signal is covered by noise (originating due to the actions of the PID system) and any periodicity with low frequencies such as the wind case can't be obtained from it (see power spectral density shown in [23] and in the appendix). On the other side, for the CF case in figure 4.13, the characteristic time of the large-scale circulation $t_0 = 14.9\,\mathrm{s}$ can be easily read. This value is not much different than the value obtained from the bulk sensor $t_0 = 14.5\,\mathrm{s}$. Because of the noisy auto-correlation functions for the constant temperature case, we can't use the signal from the temperature sensors in the bottom plate when the fast PID regulation is applied.

However, when we are approaching $Ra \sim 10^{10}$ (see figure 4.15), the first peak around the LSC period value ($\sim 15\,\mathrm{s}$) measured in the bulk starts to fade away, for $Ra < 10^9$ can be localized just with the knowledge that we have to look at this area but the certainty is small, and for even lower Ra localization is due to expanding of the central peak and then following absorption of the first peak is impossible to read value t_0.

To estimate the period of LSC t_0 from the temperature signal T_{b3} in spite of smoothing the area where the peak containing the information about t_0 is supposed to be, we can use the first visible peak. It can look like in the figure 4.16 but they must be treated very carefully, especially the values with the lowest Ra. In comparison with values obtained from the bulk temperature sensor with the same method (one probe measurement) presented in figure 9 in [25], our values agree for $Ra > 10^{11}$.

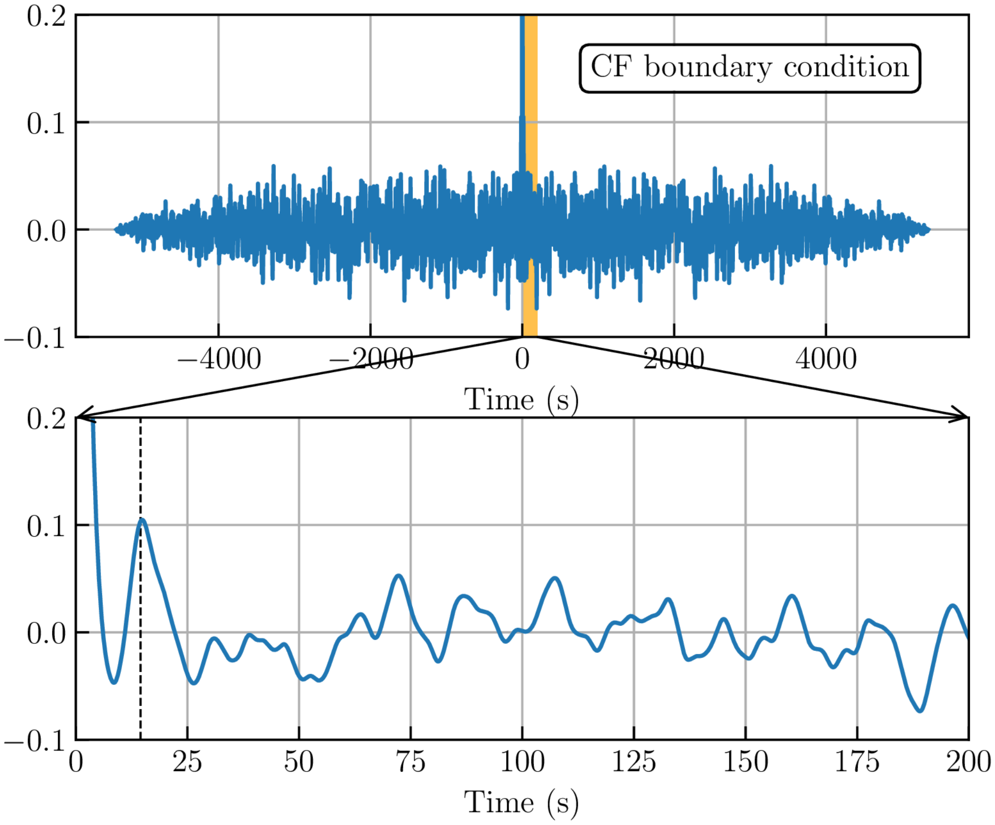

Figure 4.13: Auto-correlation function of the temperature fluctuations T_{b3} on the bottom plate at constant heat flux (CF) boundary condition on the bottom plate. Determination of the characteristic time of the large scale circulation $t_0 = 14.5\,\mathrm{s}$ is possible from the position of the first peak which can be seen in the bottom panel where a detail near the center of the auto-correlation function is displayed. Measured at $Ra \approx 1.9 \cdot 10^{12}$. Position of the first peak in the auto-correlation function of temperature recorded at the bulk sensor is represented by a dashed line.

The reason for the fading of the first peak in the auto-correlation function of the bottom plate temperature T_{b3} is not clear but it may have something to do with the thickness of the thermal boundary layer λ_{BL} (see figure 4.16). When the Ra is lower and so the Nu, the thickness of the thermal boundary layer is bigger and it might act as a shield between the plate and LSC. Also, it can be affected by the pressure p inside the cell. At low Ra, pressure p inside the cell is also lower and so the density of the helium. The ability of the LSC to move with the plate temperature is then also lower. This is also manifested in smaller thermal fluctuations as you can see in the bottom panel of figure 4.10. However, for the explanation of this phenomenon, we need to do a deeper analysis which is planned to be done subsequently, inspired by this work.

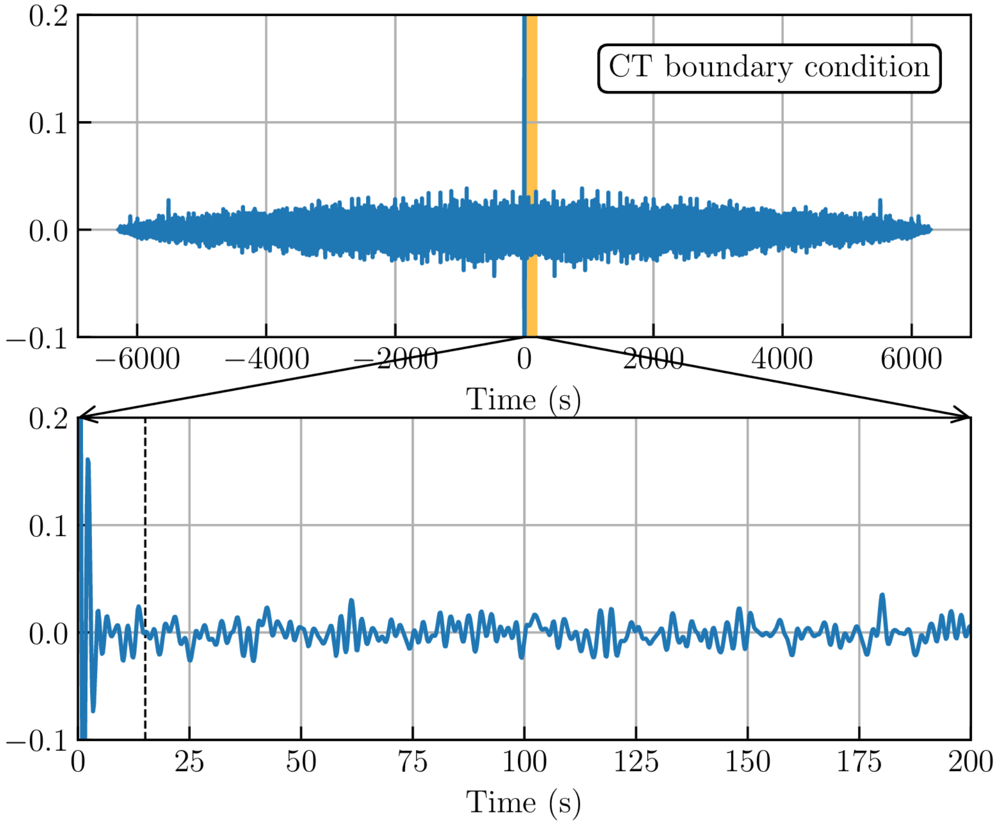

Figure 4.14: Auto-correlation function of the temperature fluctuations T_{b3} on the bottom plate at constant temperature (CT) boundary condition. The noisy behavior of the signal prevents any clear determination of the characteristic time of the large scale circulation t_0. Measured at $Ra \approx 1.9 \cdot 10^{12}$. Position of the first peak in the auto-correlation function of temperature recorded at the bulk sensor is represented by a dashed line.

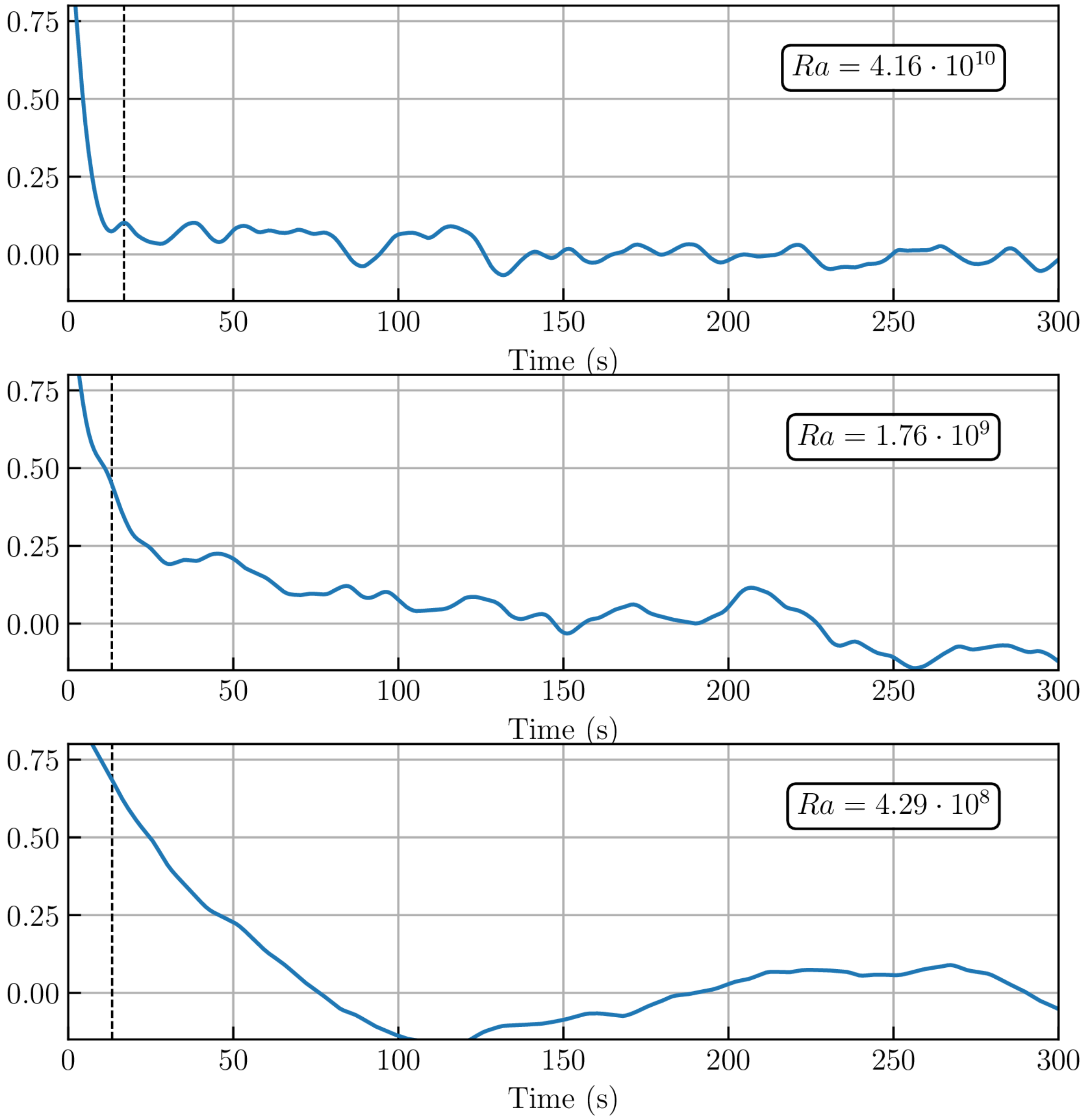

Figure 4.15: Auto-correlation functions of the temperature fluctuations of the bottom plate T_{b3} in CF regime plotted near their central maximum for three different Rayleigh numbers. Position of the first peak in the auto-correlation function of temperature recorded at the bulk sensor is represented by a dashed line.

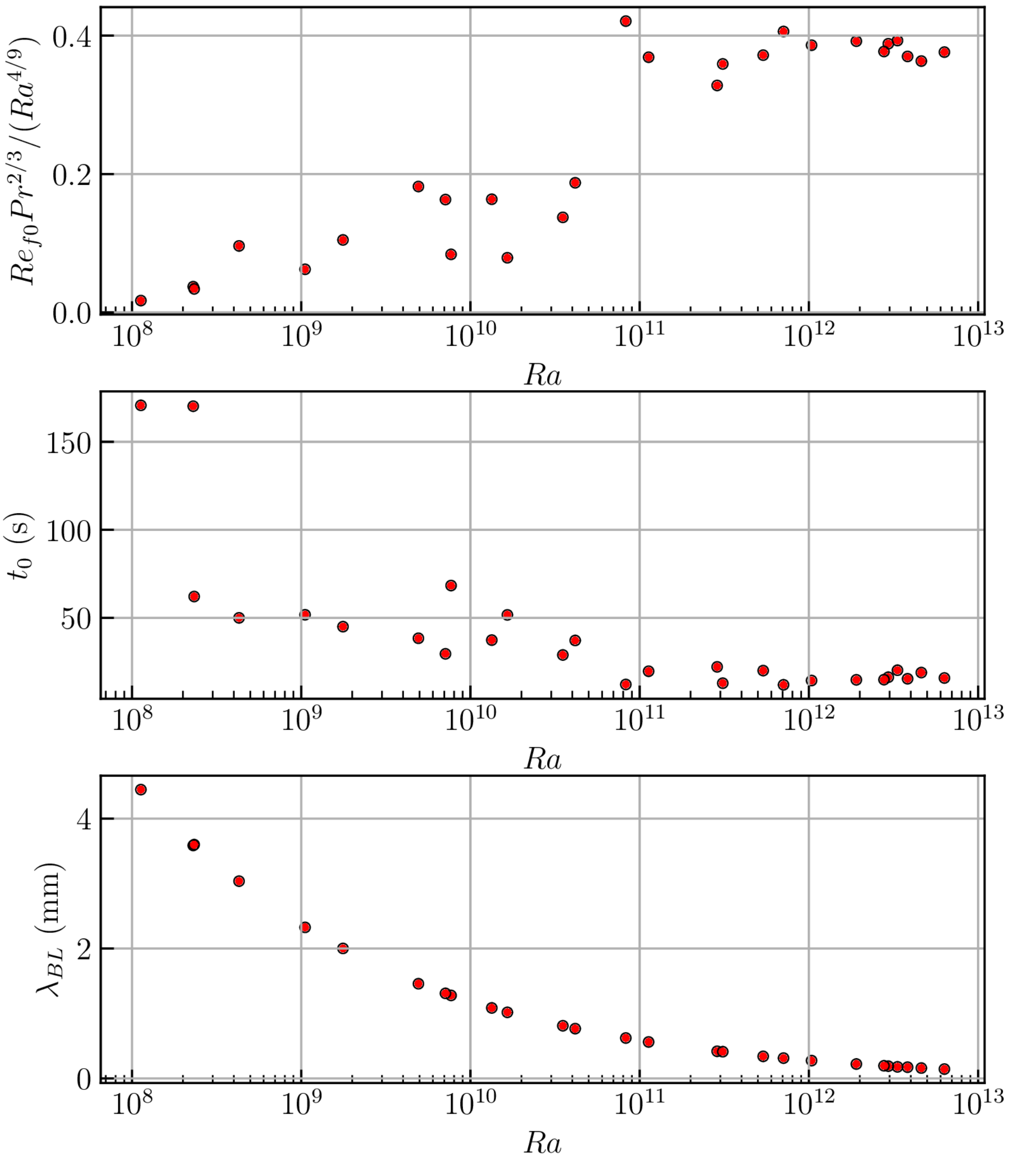

Figure 4.16: Approximate evaluation of the reduced Reynolds number Re_{f0} obtained from the equation 1.15 [25]. t_0 was estimated from the first visible peak of the autocorrelation functions of the temperature signal of the bottom plate. In the bottom panel, thickness of the thermal boundary layer λ_{BL} is evaluated.

5. Summary and conclusions

The thesis deals with the experimental study of turbulent RBC in cylindrical convection cell with aspect ratio $\Gamma = 1$ within the range of Ra numbers 10^8–$6 \cdot 10^{12}$ and the cryogenic helium gas as a working fluid. The aim was to examine in detail how effects related to boundary conditions and properties of the thermal boundary layers affect global transport properties in turbulent Rayleigh-Benard convection. In particular (i) non-Oberbeck-Boussinesq effects, related to the position of the working points in the p-T phase diagram of cryogenic helium, and (ii) the effect of the improved control of the boundary conditions were assessed. We presented the position of our working points in the p-T phase diagram in comparison with the position of working points measured in Trieste and Grenoble in figure 4.1. We followed their strategy to keep approximately constant mean temperature T_m and vary a pressure p inside the cell. In our case, $T_m \approx 5.01\,\mathrm{K}$ was kept and pressure range p varied in the range 1 kPa–152 kPa. The difference in position of the working points in the p-T phase diagram is that our measurements were performed below the liquid-vapor curve, Trieste measurements were done below the critical isochore and more close to the critical point, and Grenoble measurements were done below the critical isochore in larger distance from the critical point. We can see a possible influence of the position of the working points in the p-T phase diagram on the discrepancy among $Nu(Ra)$ dependences observed in our (Brno), Trieste, and Grenoble experiments at $Ra > 10^{11}$ (see figure 4.1 and 4.8). However, a more detailed study of this phenomenon must be done with more measurements. Notwithstanding the relatively limited sample, this work offers valuable insights into the working point position in the phase diagram.

(i) Non-Oberbeck-Boussinesq effects were studied by measuring the asymmetry between thermal boundary layers and our finding was consistent with previous measurements that we saw a rise in heat transfer efficiency when X parameter (the ratio of the temperature difference at the top and bottom boundary layer) is deflected from a value of 1. Surprisingly, we didn't see any effect on the Nusselt number Nu and X parameter when the condition $\alpha\Delta T < 0.2$ serving as the condition for the Oberbeck-Boussinesq approximation was exceeded for a few Rayleigh numbers Ra. However, the fluid properties varied significantly (see figure 4.5). This can indicate the insufficiency of this condition and observations of this thesis will be developed in the identification of criteria more sensitively evaluating the influence of NOB effects on RBC.

(ii) The next section of the study was concerned with the effect of thermal boundary conditions on the bottom plate. A clear difference between the constant heat flux (CF) regime and constant temperature (CT) regime can be seen in figures 4.10 and 4.11 displaying the magnitude of temperature fluctuations at both top/bottom plates and in the bulk. However, the effect on the Nusselt number Nu is none which is consistent with [9, 10]. On the topic of thermal boundary conditions was also written the Letter [23] which is in the appendix of this thesis. In extension to this thesis, there is comparison of our cryogenic experiment with experiments using water and SF_6 as a working fluid, power spectral densities of the plates, Reynolds numbers Re_p evaluated from the two probe measurement and the reversals of the large scale circulation (LSC).

The Reynolds number Re is usually evaluated from the thermal sensors in the bulk of Rayleigh-Bénard convection. In the final part, we present the evaluation of the Reynolds number Re by using a thermal sensor on the outer side of the bottom plate. For the CT regime, it was impossible to detect the period of the LSC t_0 needed for the Re but in the CF regime, a clear first peak in the auto-correlation function indicating the period of the LSC t_0 is visible and its position corresponds with position when the auto-correlation function is calculated from the bulk sensor. What is surprising is the fading of this first peak with decreasing Ra resulting in no possible correct evaluation of the t_0 for $Ra <\sim 10^{10}$. A possible explanation for this might be the growing thickness of the thermal boundary layer λ_{BL}. In this case, the thermal boundary layer λ_{BL} can function as a shield so the LSC can not much influence the bottom plate. Another possible explanation for this is that lower Ra were measured with lower pressures p and so with a lesser amount of the fluid resulting in its small thermal capacity. Then, when the LSC hits the bottom plate, the influence is not so big because the heat removed from the bottom plate is small.

Bibliography

1. CHILLÀ, F.; SCHUMACHER, J. New perspectives in turbulent Rayleigh-Bénard convection. *The European Physical Journal E.* 2012, vol. 35, no. 7. ISSN 1292-8941. Available from DOI: `10.1140/epje/i2012-12058-1`.
2. URBAN, P. et al. Effect of Boundary Layers Asymmetry on Heat Transfer Efficiency in Turbulent Rayleigh-Bénard Convection at Very High Rayleigh Numbers. *Physical Review Letters* [online]. 2012, vol. 109, no. 15 [visited on 2019-04-20]. ISSN 0031-9007. Available from DOI: `10.1103/PhysRevLett.109.154301`.
3. URBAN, P.; MUSILOVÁ, V.; SKRBEK, L. Efficiency of Heat Transfer in Turbulent Rayleigh-Bénard Convection. *Physical Review Letters* [online]. 2011, vol. 107, no. 1 [visited on 2021-04-27]. ISSN 0031-9007. Available from DOI: `10.1103/PhysRevLett.107.014302`.
4. URBAN, Pavel et al. Heat transfer in cryogenic helium gas by turbulent Rayleigh–Bénard convection in a cylindrical cell of aspect ratio 1. *New Journal of Physics* [online]. 2014, vol. 16, no. 5, p. 053042 [visited on 2019-04-22]. ISSN 1367-2630. Available from DOI: `10.1088/1367-2630/16/5/053042`.
5. URBAN, P. et al. Elusive transition to the ultimate regime of turbulent Rayleigh-Bénard convection. *Physical Review E* [online]. 2019, vol. 99, no. 1 [visited on 2021-04-24]. ISSN 2470-0045. Available from DOI: `10.1103/PhysRevE.99.011101`.
6. ROCHE, P.-E. et al. Side wall effects in Rayleigh Bénard experiments. *The European Physical Journal B* [online]. 2001, vol. 24, no. 3, pp. 405–408 [visited on 2021-04-24]. ISSN 1434-6028. Available from DOI: `10.1007/s10051-001-8690-5`.
7. GOLUSKIN, David. *Internally Heated Convection and Rayleigh-Bénard Convection* [online]. Cham: Springer International Publishing, 2016 [visited on 2021-05-11]. ISBN 978-3-319-23939-2. Available from DOI: `10.1007/978-3-319-23941-5`.
8. VERZICCO, R.; SREENIVASAN, K. R. A comparison of turbulent thermal convection between conditions of constant temperature and constant heat flux. *Journal of Fluid Mechanics* [online]. 2008, vol. 595, pp. 203–219 [visited on 2021-04-24]. ISSN 0022-1120. Available from DOI: `10.1017/S0022112007009135`.
9. STEVENS, RICHARD J. A. M.; VERZICCO, ROBERTO; LOHSE, DETLEF. Radial boundary layer structure and Nusselt number in Rayleigh–Bénard convection. *Journal of Fluid Mechanics* [online]. 2010, vol. 643, pp. 495–507 [visited on 2021-05-11]. ISSN 0022-1120. Available from DOI: `10.1017/S0022112009992461`.
10. JOHNSTON, Hans; DOERING, Charles R. Comparison of Turbulent Thermal Convection between Conditions of Constant Temperature and Constant Flux. *Physical Review Letters* [online]. 2009, vol. 102, no. 6 [visited on 2021-05-09]. ISSN 0031-9007. Available from DOI: `10.1103/PhysRevLett.102.064501`.
11. HUANG, Shi-Di et al. Comparative Experimental Study of Fixed Temperature and Fixed Heat Flux Boundary Conditions in Turbulent Thermal Convection. *Physical Review Letters* [online]. 2015, vol. 115, no. 15 [visited on 2021-04-24]. ISSN 0031-9007. Available from DOI: `10.1103/PhysRevLett.115.154502`.

12. TRITTON, D.J. *Physical Fluid Dynamics.* 2 ed. Oxford: Clarendon Press, 1988. ISBN 0-19-854493-6.
13. CHERKASHIN, I.; PUCKETT, E. *Derivation of the Rayleigh–Bénard equations for modeling convection in the Earth's mantle (Long version)* [online]. 2016 [visited on 2021-04-24]. Available from: `https://www.researchgate.net/publication/294428344_Derivation_of_the_Rayleigh-Benard_equations_for_modeling_convection_in_the_Earth's_mantle_Long_version`.
14. CHAVANNE, X. et al. High rayleigh number convection with gaseous helium at low temperature. *Journal of Low Temperature Physics* [online]. 1996, vol. 104, no. 1-2, pp. 109–129 [visited on 2019-04-22]. ISSN 0022-2291. Available from DOI: `10.1007/BF00754092`.
15. AHLERS, Guenter; GROSSMANN, Siegfried; LOHSE, Detlef. Heat transfer and large scale dynamics in turbulent Rayleigh-Bénard convection. *Reviews of Modern Physics* [online]. 2009, vol. 81, no. 2, pp. 503–537 [visited on 2019-04-22]. ISSN 0034-6861. Available from DOI: `10.1103/RevModPhys.81.503`.
16. SHRAIMAN, Boris I.; SIGGIA, Eric D. Heat transport in high-Rayleigh-number convection. *Physical Review A* [online]. 1990, vol. 42, no. 6, pp. 3650–3653 [visited on 2019-05-08]. ISSN 1050-2947. Available from DOI: `10.1103/PhysRevA.42.3650`.
17. CASTAING, Bernard et al. Scaling of hard thermal turbulence in Rayleigh-Bénard convection. *Journal of Fluid Mechanics* [online]. 1989, vol. 204, no. -1 [visited on 2021-04-24]. ISSN 0022-1120. Available from DOI: `10.1017/S0022112089001643`.
18. SKRBEK, L.; URBAN, P. Has the ultimate state of turbulent thermal convection been observed? *Journal of Fluid Mechanics* [online]. 2015, vol. 785, pp. 270–282 [visited on 2019-05-09]. ISSN 0022-1120. Available from DOI: `10.1017/jfm.2015.638`.
19. RICHARDSON, S. On the no-slip boundary condition. *Journal of Fluid Mechanics* [online]. 1973, vol. 59, no. 4, pp. 707–719 [visited on 2021-04-24]. ISSN 0022-1120. Available from DOI: `10.1017/S0022112073001801`.
20. BROWN, Eric et al. Heat transport in turbulent Rayleigh-Bénard convection: Effect of finite top- and bottom-plate conductivities. *Physics of Fluids* [online]. 2005, vol. 17, no. 7 [visited on 2021-04-24]. ISSN 1070-6631. Available from DOI: `10.1063/1.1964987`.
21. STEVENS, Richard J. A. M.; LOHSE, Detlef; VERZICCO, Roberto. Prandtl and Rayleigh number dependence of heat transport in high Rayleigh number thermal convection. *Journal of Fluid Mechanics* [online]. 2011, vol. 688, pp. 31–43 [visited on 2021-05-09]. ISSN 0022-1120. Available from DOI: `10.1017/jfm.2011.354`.
22. DRAHOTSKÝ, Jakub et al. Temperature profiles measurements in turbulent Rayleigh-Bénard convection by optical fibre system at the Barrel of Il-menau. *EPJ Web of Conferences* [online]. 2018, vol. 180, p. 02020 [visited on 2021-05-13]. ISSN 2100-014X. Available from DOI: `10.1051/epjconf/201818002020`.
23. URBAN, P. et al. *Effect of boundary conditions in turbulent thermal convection.* 2021. Available from arXiv: `2105.02740 [physics.flu-dyn]`.

24. CHENG, Yu et al. Failure of Taylor's hypothesis in the atmospheric surface layer and its correction for eddy-covariance measurements. *Geophysical Research Letters* [online]. 2017, vol. 44, no. 9, pp. 4287–4295 [visited on 2021-05-13]. ISSN 00948276. Available from DOI: `10.1002/2017GL073499`.
25. MUSILOVÁ, Věra et al. Reynolds number scaling in cryogenic turbulent Rayleigh–Bénard convection in a cylindrical aspect ratio one cell. *Journal of Fluid Mechanics* [online]. 2017, vol. 832, pp. 721–744 [visited on 2021-05-09]. ISSN 0022-1120. Available from DOI: `10.1017/jfm.2017.638`.
26. THRELFALL, D. C. Free convection in low-temperature gaseous helium. *Journal of Fluid Mechanics* [online]. 1975, vol. 67, no. 1, pp. 17–28 [visited on 2021-05-09]. ISSN 0022-1120. Available from DOI: `10.1017/S0022112075000158`.
27. NIEMELA, J. J. et al. Turbulent convection at very high Rayleigh numbers. *Nature* [online]. 2000, vol. 404, no. 6780, pp. 837–840 [visited on 2021-04-24]. ISSN 0028-0836. Available from DOI: `10.1038/35009036`.
28. VĚŽNÍK, T. *Role of thermal near field in cryogenic Rayleigh-Bénard convection* [online]. Brno, 2019 [visited on 2021-05-09]. Bachelor's thesis. Brno University of Technology, Faculty of Mechanical Engineering. Supervised by Ph.D ING. PAVEL URBAN.
29. ROCHE, P-E et al. On the triggering of the Ultimate Regime of convection. *New Journal of Physics* [online]. 2010, vol. 12, no. 8, p. 085014 [visited on 2019-05-08]. ISSN 1367-2630. Available from DOI: `10.1088/1367-2630/12/8/085014`.
30. URBAN, Pavel. *Helium Cryostat for Experimental Study of Natural Turbulent Convection* [online]. Brno, 2010 [visited on 2021-05-09]. Available from: `http://hdl.handle.net/11012/7789`. PhD thesis. Brno University of Technology, Faculty of Mechanical Engineering.
31. MITIN, V.F. et al. Ge-on-GaAs film resistance thermometers for cryogenic applications. *Cryogenics* [online]. 2007, vol. 47, no. 9-10, pp. 474–482 [visited on 2021-05-13]. ISSN 00112275. Available from DOI: `10.1016/j.cryogenics.2007.04.014`.
32. ARP, V.D.; MCCARTY, R.D. *HEPAK 3.40/3.41 – User's Guide*. Horizon Technologies, 2005. Available also from: `https://htess.com`.
33. NIEMELA, J. J.; SREENIVASAN, K. R. Confined turbulent convection. *Journal of Fluid Mechanics* [online]. [N.d.], vol. 481, pp. 355–384 [visited on 2019-04-22]. ISSN 00221120. Available from DOI: `10.1017/S0022112003004087`.

List of symbols, physical constants and abbreviations

Ra	Rayleigh number
Pr	Prandtl number
Nu	Nusselt number
Re	Reynolds number
Re_{f0}	Frequency Reynolds number
Re_p	Two-point Reynolds numbers
Γ	Aspect ratio
L	Height of the cell
D	Diameter of the cell
S	Area of the plate or the plume
λ_{BL}	Thickness of the boundary layer
d	Distance between two probes
T	Temperature
T_t	Temperature of the top plate
T_b	Temperature of the bottom plate
T_m	Mean temperature
T_c	Temperature of the bulk
ΔT	Temperature difference between the plates
Δ_t	Temperature difference on the top boundary layer
Δ_b	Temperature difference on the bottom boundary layer
δT	Temperature fluctuation
σT	Standard deviation of the temperature
$\vec{u}$	Flow velocity
t	Time
p	Pressure
$\vec{g}$	Gravitional acceleration

$\vec{q}$	Heat flux
q_{cond}	Conductive heat flux
Q_b, Q_t	Power of the bottom and the top heater respectively
ρ	Fluid density
μ	Dynamic viscosity of the fluid
λ	Thermal conductivity of the fluid
κ	Thermal diffusivity of the fluid
α	Coefficient of thermal expansion of the fluid
ν	Kinematic viscosity of the fluid
FP	Fluid property
FP_c, FP_t, FP_b	Fluid property at temperatures T_c, T_t, T_b respectively
C_p	Isobaric thermal capacity of the fluid
λ_{pl}	Thermal conductivity of the plate
C_{pl}	Thermal capacity of the plate
rho_pl	Density of the fluid
γ	Scaling exponent in $Nu(Ra)$ dependence
X	X parameter defined in equation 1.13
X_{th}	Theoretical X parameter defined in equation 1.14
K	K parameter defined in section 1.6
t_0	Specific turnover time of the wind
τ_p	Time delay between signals from cross-correlations
RBC	Rayleigh-Bénard convection
ISI	Institute of Scientific Instruments
ConEV	Convection Experimental Vessel
CoCoS	Convection Control System
HeTWiCA	Helium Turbulent Wind Control and Acquisition
BL	Thermal Boundary Layer
CF	Constant Heat Flux

CT	Constant Temperature
OB	Oberbeck-Boussinesq
LSC	Large scale circulation
PID	Proportional-Integral-Derivative
PDF	Probability density function

Appendix

Effect of boundary conditions in turbulent thermal convection

P. Urban[1], T. Králík[1], M. Macek[1], P. Hanzelka[1], T. Věžník[1] and L. Skrbek[2]

[1] *The Czech Academy of Sciences, Institute of Scientific Instruments, Královopolská 147, Brno, Czech Republic*
[2] *Faculty of Mathematics and Physics, Charles University, Ke Karlovu 3, Prague, Czech Republic*

arXiv:2105.02740v1 [physics.flu-dyn] 6 May 2021

PACS `47.27.-i` – Turbulent flows
PACS `47.55.pb` – Thermal convection
PACS `47.27.te` – Turbulent convective heat transfer

Abstract. - We report an experimental study aiming to clarify the role of boundary conditions (BC) in high Rayleigh number $10^8 < \mathrm{Ra} < 3 \times 10^{12}$ turbulent thermal convection of cryogenic helium gas. We switch between BC closer to constant heat flux (CF) and constant temperature (CT) applied to the highly conducting bottom plate of the aspect ratio one cylindrical cell 30 cm in size, leading to dramatic changes in the temperature probability density function and in power spectral density of the temperature fluctuations measured at the bottom plate, while the dynamic thermal behaviour of the top plate and bulk convective flow remain unaffected. Within our experimental accuracy, we find no appreciable changes in Reynolds number Re(Ra) scaling, in the dimensionless heat transfer efficiency expressed via Nusselt number Nu(Ra) scaling, nor in the rate of direction reversals of large scale circulation.

Introduction. – Confined 3D turbulent Rayleigh-Bénard convection (RBC) [1,2] serves as a model system on our way to understand many natural phenomena and represents the most frequently studied thermally driven turbulent flow. The ideal laterally infinite RBC occurs in a fluid layer confined between two horizontal, perfectly conducting plates heated from below in a gravitational field, and for an Oberbeck-Boussinesq (OB) fluid it is fully characterized by the Rayleigh (Ra) and the Prandtl (Pr) numbers. The convective heat transfer efficiency is described by the Nusselt number, via the Nu = Nu(Ra; Pr) dependence. Large scale circulation (LSC), also known as 'wind' [3] of mean velocity U and dimension of the size of the convective layer, L (or the size D of the RBC cell in the case of laterally confined RBC) is known to exist in RBC and can be characterized by the Reynolds number (Re). The dimensionless numbers describing confined RBC are defined as:

$$\mathrm{Nu} = \frac{Lq}{\lambda_f \Delta T};\ \mathrm{Ra} = \frac{g\alpha_f}{\nu_f \kappa_f}\Delta T L^3;\ \mathrm{Pr} = \frac{\nu_f}{\kappa_f};\ \mathrm{Re} = \frac{UL}{\nu_f}. \tag{1}$$

Here q is the total convective heat flux density, g stands for the acceleration due to gravity, and ΔT is the temperature difference between the parallel top and bottom plates separated by the vertical distance L. The properties of the working fluid are characterized by the thermal conductivity, λ_f, and by the combination $\alpha_f/(\nu_f \kappa_f)$, where α_f is the isobaric thermal expansion, ν_f is the kinematic viscosity, and κ_f denotes the thermal diffusivity; $\kappa_f = \lambda_f/(\rho_f c_{pf})$, where ρ_f is the density and c_{pf} specific heat of the working fluid at constant pressure. In the laboratory the RBC experiments often take place in cylindrical cells of diameter D and height L; the relevant additional parameter is the aspect ratio defined as $\Gamma = D/L$, which might be understood as a first approximation in taking into account the shape of the RBC cell.

From the **theoretical/numerical** point of view, within the OB approximation and assuming that the flow is incompressible, the 3D RBC is fully described by well-known equations of motion [1,2] which, however, must be complemented with the boundary conditions (BC's). While for the velocity field the no-slip BC [4] on all inner surfaces of the RBC cell are taken as justified, the BC's for the temperature field can be expressed, for example, in the Dirichlet form – constant temperature (CT) of the solid-fluid boundary or as a constant heat flux (CF) supplied via entire area of the bottom of the RBC cell [5,6].

In **experimental** studies of RBC, however, the temperature BC's at the interface between the fluid and the plate are always a combination of CT and CF. The main motivation of our study is that their relative weight can be, up to some degree, experimentally adjusted *in situ.* There are many experimental parameters that affect the RBC flow under study. Following our earlier work [7],

Table 1: Experimental quantities relevant for generation of cryogenic turbulent RBC flows in the Brno experimental cell [14] in comparison with hypothetical RBC flows of the same Ra and Nu (assuming the same Nu=Nu(Ra) scaling) that would be requested at ambient temperatures using H_2O and SF_6 as working fluids [15–17]. The $\Gamma = 1$ Brno cell has $e = 28$ mm thick top and bottom plates 30 cm in diameter made of annealed copper of thermal conductivity λ_p=2210 and 400 W $\mathrm{m}^{-1}\mathrm{K}^{-1}$ and thermal capacity $c_p = 0.144$ and 386 J $\mathrm{kg}^{-1}\mathrm{K}^{-1}$ at $T_m = (T_t + T_b)/2 \approx 5$ K and 300 K, respectively [18]. The influence of the vertical wall, made of nominally 0.5 mm thick stainless steel, is neglected. For definition of the displayed physical quantities $\alpha_f \Delta T, Q_b, \frac{\lambda_p}{\mathrm{Nu}\lambda_\mathrm{f}}, \tau_p^h, \tau_f^h, \ell_p, K, \tau_\mathrm{plm}, \tau_\mathrm{plt}$, see the text.

	unit	He	H_2O	SF_6	He	H_2O	SF_6	He	SF_6
Ra	1	$2.3\text{x}10^{8}$	$2.3\text{x}10^{8}$	$2.3\text{x}10^{8}$	$1.3\text{x}10^{10}$	$1.3\text{x}10^{10}$	$1.3\text{x}10^{10}$	$2.2\text{x}10^{12}$	$2.2\text{x}10^{12}$
Nu	1	41.7	41.7	41.7	138.3	138.3	138.3	717.8	717.8
Pr	1	0.68	5.85	0.79	0.71	5.85	0.79	1.00	0.86
T_m	K	5.009	300.0	300.0	5.016	300.0	300.0	5.009	300.0
ΔT	K	1.027	0.402	8.936	0.183	23.08	12.32	0.196	16.19
P	Pa	$1.03\text{x}10^{3}$	$1.00\text{x}10^{5}$	$5.00\text{x}10^{5}$	$1.74\text{x}10^{4}$	$1.00\text{x}10^{5}$	$3.00\text{x}10^{5}$	$1.21\text{x}10^{5}$	$1.8\text{x}10^{6}$
ν_f	$\frac{\mathrm{m}^2}{\mathrm{s}}$	$1.26\text{x}10^{-5}$	$8.57\text{x}10^{-7}$	$5.21\text{x}10^{-6}$	$7.4\text{x}10^{-7}$	$8.57\text{x}10^{-7}$	$8.46\text{x}10^{-7}$	$9.50\text{x}10^{-8}$	$1.2\text{x}10^{-7}$
κ_f	$\frac{\mathrm{m}^2}{\mathrm{s}}$	$1.85\text{x}10^{-5}$	$1.46\text{x}10^{-7}$	$6.62\text{x}10^{-6}$	$1.04\text{x}10^{-6}$	$1.46\text{x}10^{-7}$	$1.08\text{x}10^{-6}$	$9.47\text{x}10^{-8}$	$1.4\text{x}10^{-7}$
α_f	1/K	$2.00\text{x}10^{-1}$	$2.75\text{x}10^{-4}$	$3.40\text{x}10^{-3}$	$2.13\text{x}10^{-1}$	$2.75\text{x}10^{-4}$	$3.74\text{x}10^{-3}$	$3.79\text{x}10^{-1}$	$8.4\text{x}10^{-3}$
λ_f	$\frac{\mathrm{W}}{\mathrm{m\ K}}$	$9.57\text{x}10^{-3}$	$6.10\text{x}10^{-1}$	$1.30\text{x}10^{-2}$	$9.65\text{x}10^{-3}$	$6.10\text{x}10^{-1}$	$1.32\text{x}10^{-2}$	$1.05\text{x}10^{-2}$	$1.5\text{x}10^{-2}$
ρ_f	$\frac{\mathrm{kg}}{\mathrm{m}^3}$	0.10	996.6	2.94	1.72	996.6	18.19	15.03	139.2
c_{pf}	$\frac{\mathrm{J}}{\mathrm{kg\ K}}$	5203	4181	667.9	5372	4181	673.5	7367	784.7
$\alpha_f \Delta T$	1	$2.10\text{x}10^{-1}$	$1.10\text{x}10^{-4}$	$3.00\text{x}10^{-2}$	$3.90\text{x}10^{-2}$	$6.30\text{x}10^{-3}$	$4.6\text{x}10^{-2}$	$7.4\text{x}10^{-2}$	$1.4\text{x}10^{-1}$
Q_b	W	0.095	2.410	1.142	0.056	458.8	5.291	0.344	41.46
$\frac{\lambda_p}{\mathrm{Nu}\lambda_f}$	1	5539	15.7	737	1656	4.7	219.3	293.8	36.8
τ_p^h	s	27.6	1140	53444	8.3	343.5	15904	1.5	2668
τ_f^h	s	59.3	7372	163.1	321.2	2222	302.4	668.2	452.4
ℓ_p	mm	1.445	4.344	0.002	7.787	1.309	0.004	17.97	0.007
K	1	$1.38\text{x}10^{4}$	13.0	$1.29\text{x}10^{6}$	231	3.9	$6.18\text{x}10^{4}$	3.4	1162
τ_plm	s	1.8	5.3	1.9	1.3	3.7	1.3	0.7	0.7
τ_plt	s	$1.2\text{x}10^{-3}$	$4.1\text{x}10^{-1}$	6.7	$5.2\text{x}10^{-4}$	3.1	8.3	$7.1\text{x}10^{-4}$	$1.4\text{x}10^{1}$
$\frac{\tau_\mathrm{plt}}{\tau_\mathrm{plm}}$	1	$6.5\text{x}10^{-4}$	$7.7\text{x}10^{-2}$	3.5	$4.1\text{x}10^{-4}$	8.4	6.2	$9.9\text{x}10^{-4}$	$2.1\text{x}10^{1}$

we could loosely divide them into two groups: geometrical and physical. The first group includes the actual size and shape of the cell (e.g., rectangular or cylindrical), thickness of walls and plates, their surface roughness or possible deviation from the horizontal position. The second group includes the actual physical properties of the working fluid as well as of construction materials of the RBC cell, such as thermal conductivity and heat capacity of plates($\lambda_p; c_p$) and walls, the thermal conductivity of the electrical leads and, generally, the physical properties of the surrounding medium. Although various approaches to correct the raw data with respect to finite thermal conductivity of plates [8] and walls [9], parasitic heat leaks, adiabatic thermal gradient, thermal radiation [10] or non OB effects [7,11–13] have been attempted by various authors, it is generally very difficult if not impossible to fully eliminate all these factors. In order to single out and appreciate the role of BC on the RBC flow under study, it therefore seems the best to perform the experiment under the same conditions while changing the BC only.

On the other hand, we believe that it is instructive to compare, for selected RBC flows fully described by Ra, Pr and $\Gamma = 1$, also additional parameters relevant for a typical RBC experiment assuming it performed in the same cell. We have chosen three typical data points measured in this study with cryogenic He gas (see Table 1) that belong to ranges of Ra obeying power scaling $\mathrm{Nu} = \mathrm{Nu}(\mathrm{Ra}) \propto \mathrm{Ra}^\gamma$ ($\gamma \approx 2/7$, crossover regime and $\gamma \approx 1/3$ [7,19]) and compare them with complementary hypothetical turbulent RBC flows, assuming them generated in the same cell at ambient temperatures using frequently used working fluids: H_2O and SF_6. The numerical value $\alpha_f \Delta T <\approx 0.2$ is conventionally understood as a satisfactory OB criterion. The thickness of the thermal boundary layer $\ell_\mathrm{BL} = L/(2\mathrm{Nu})$ is naturally the same for the same Nu, however, the heat currents $Q_b = qS_p$ (S_p being the plate area) required to be applied to the bottom plate are for complementary RBC flows very different. It would take the time τ_p^h to heat just the bottom plate alone (assuming it thermally isolated) by ΔT, and time τ_f^h to heat the working fluid by $\Delta T/2$, i.e., to the temperature of turbulent bulk of the RBC flow. An important factor is the heat conductivity, λ_p, of the plates. Its influence on Nu was thoroughly studied [8,20] and experimentally confirmed by Brown *et al.* [21], who used H_2O in otherwise identical RBC cells with Cu ($\lambda_p \approx 391$ $\mathrm{Wm^{-1}K^{-1}}$) and Al ($\lambda_p \approx 161$ $\mathrm{Wm^{-1}K^{-1}}$) plates and concluded that low λ_p appreciably diminishes the heat transport efficiency, at least in RBC cells of size similar to our own [14]. An important requirement is that the ratio $\lambda_p/(\mathrm{Nu}\lambda_f)$ is high, which for Cu plates and water is low (see Table 1) but even lower for Al plates. Note that for SF_6 and especially for cryogenic He this ratio is about two (three) orders of magnitude higher.

The key role for establishing the ratio of CT versus CF BC's is played by thermal plumes. Let us consider a typical plume: a two-dimensional sheet-like structure of temperature $\approx T_b$ (hot plume) or $\approx T_t$ (cold plume) and thickness comparable to ℓ_{BL}, which initially extends in the vertical direction, eventually to be bent by LSC. If such a plume of area S abruptly detaches, it takes with it (leaves behind) heat $Q_p \approx S\ell_{\mathrm{BL}}c_f\rho_f\Delta T/2$, equivalent to a thermal hole in the plate, of thickness $\ell_p \approx 2Q_p/(S\Delta T c_p\rho_p)$ (see Table 1); this thermal hole must be refilled using the heat flux delivered by a heater via thermal conduction of the plate. From this point of view, an important parameter is $K = (\rho_p c_p \lambda_p)/(\rho_f c_f Nu \lambda_p)$ [22]. The characteristic time between two successive plumes has been estimated by Castaing *et al.* [23] as $\tau_{\mathrm{plm}} = (\mathrm{RaPr})^{1/2}/(4\mathrm{Nu}^2)$. It decreases with Ra, since Nu increases faster than $\mathrm{Ra}^{1/4}$. To assure CT BC the plate should be fast enough to provide consecutive plumes with enough heat by thermal diffusion, which occurs within a characteristic time $\tau_{\mathrm{plt}} = (\mathrm{RaPr})^{1/2}(e/L)^2(\kappa_f/\kappa_p)$ [20,23]. This means that CT BC will be better achieved if K is big and the ratio $\tau_{\mathrm{plt}}/\tau_{\mathrm{plm}}$ is small, which is out of the three considered cases best achieved for cryogenic He.

Experiment. In order to appreciate the role of BC on RBC flow, we perform the experiment under nominally the same conditions while switching on and off the PID-stabilizing scheme of the bottom plate temperature T_b. We use the updated version of the Brno experimental cell [14], shown in Fig. 1. Essential improvements are the following: (i) the original mid flanges on the sidewall have been gradually deformed in previous experiments and found prone to leakage at high pressure of the working fluid; these flanges were therefore replaced and the joints welded together; (ii) several small Ge temperature sensors (Ge-on-GaAs film resistance thermometers, [24]) attached to tightly stretched thin constantan wires have been installed, via newly made sidewall feedthroughs; their geometrical positions are shown in Fig. 1; and (iii) in addition to the precisely calibrated stable Ge sensors embedded in the plates, fast DT-670 Silicon Diodes (Lake Shore) have been attached to both plates.

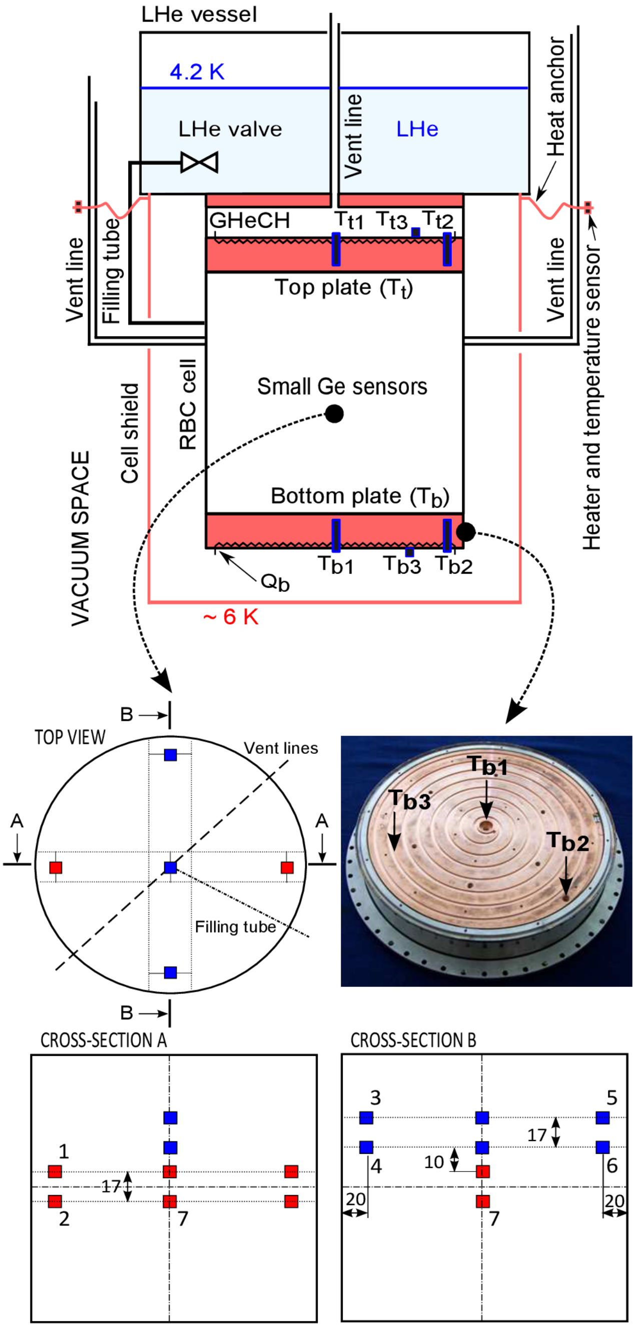

Fig. 1: The sketch of the Brno RBC cell. From the top plate, most of heat is removed via the He gas heat exchange chamber (GHeCH) to liquid He vessel above it. T_t is roughly set by pressure in the GHeCH and more precisely by the distributed heater. Note the positions (distances in mm) of small Ge sensors (numbered are those used in this study) in the cell interior, the finely calibrated Ge sensors $\mathrm{T_{t1}, T_{t2}, T_{b1}}$ and $\mathrm{T_{b2}}$ embedded in the plates and two fast diodes $\mathrm{T_{t3}}$ and $\mathrm{T_{b3}}$ at the outer surfaces of plates (see the detail of the bottom plate, showing the spiral grove where the heater is glued, delivering approximately uniformly both the heat flux q and the PID-control heat flux aimed to stabilize T_b.

Due to rather complex thermal connection of the top plate with the liquid helium vessel above it, partly via a stainless steel sidewall but mainly via the He gas heat exchange chamber (GHeCH) which itself represents a con-

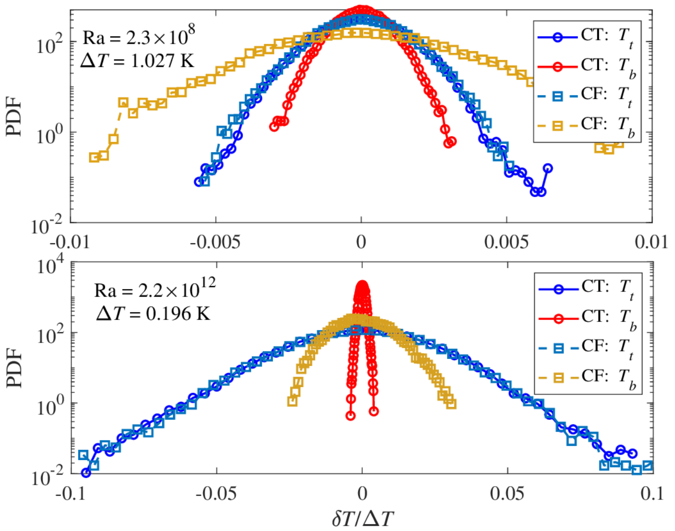

Fig. 2: Examples of the PDFs of the temperatures $T_b(t)$ and $T_t(t)$ fluctuating about mean temperatures $\langle T_b\rangle$ and $\langle T_t\rangle$, measured by fast responding diodes $\mathrm{T_{b3}}$ and $\mathrm{T_{t3}}$ placed at the outside horizontal surfaces of the bottom and top plates at Ra as indicated, for two sets of BC discussed in the text. The PID control of the bottom plate temperature results in significantly narrower PDFs (red circles), in comparison with "standard" CF heating (orange squares), while the PDFs measured at the top plate (blue symbols) remain unaffected.

vection cell, we have focused on changing BC at the bottom plate and compare two distinctly different cases. In both of them, the heat is supplied to the bottom plate via a distributed wire heater. As the distance between heater turns is smaller than the plate thickness, the heat delivered to its upper surface, in the absence of convective flow in the RBC cell, can be thought of as steady and uniformly distributed. Turbulent RBC flow breaks this symmetry both in time and space. Although the total heat flux delivered by the resistive heater to the outer side of the bottom plate remains constant, due to thermal plumes detachment and dynamical thermal properties of the bottom plate, the CF BC is not strictly valid at the bottom solid-fluid boundary of the RBC flow. Despite this caveat, also in view of numerical studies such as [25], hereafter we call this Case 1 as CF BC.

We note that delivering constant heat flux (CF) to the outer side of bottom plate while controlling the mean top plate temperature (via adjusting the pressure in the exchange chamber and, additionally, by fine tuning via uniformly distributed resistive heater glued in the spiral grove on the upper surface of the top plate achieved by using a PID control) is the "standard" way of generating statistically steady turbulent RBC flows studied in our previous experiments [7, 19, 26, 27] and references therein.

Case 2 to compare with, hereafter called CT BC, differs in that the bottom plate heater is included in the PID control feedback loop, designed to keep the temperature of the bottom plate stable. The PID scheme uses the reference signal from the fast-responding diode $\mathrm{T_{b3}}$. In both cases, the mean temperature difference $\Delta T = \langle T_b\rangle - \langle T_t\rangle$ is kept constant, where the mean temperatures $\langle T_b\rangle$ and $\langle T_t\rangle$ are accurately determined by finely calibrated Ge sensors $\mathrm{T_{b1}}$, $\mathrm{T_{b2}}$ and $\mathrm{T_{t1}}$, $\mathrm{T_{t2}}$. The fluctuating values $T_b(t)$ and $T_t(t)$ are monitored by home-calibrated diodes $\mathrm{T_{b3}}$ and $\mathrm{T_{t3}}$, and the temperature fluctuations $T_N(t)(N = 1...12)$ in various places of the cell interior by small Ge-on-GaAs film sensors [24].

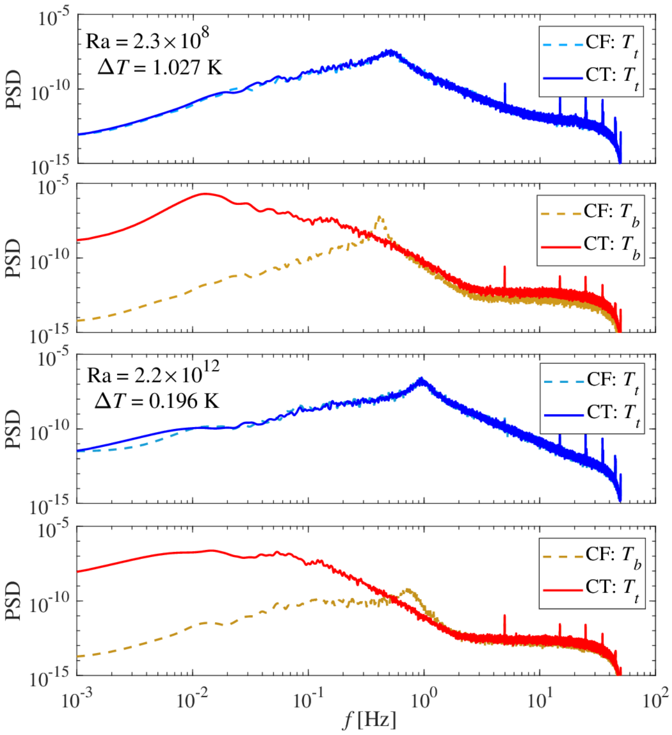

Fig. 3: PSDs of the fluctuating temperature calculated for the cases shown in Fig. 2 display significant depletion at frequencies below 0.4 Hz (0.7 Hz) for the lower (higher) Ra cases; faster temperature fluctuations of the bottom plate are hardly affected by the PID control (red lines). At the top plate, PSDs (blue lines) remain entirely unaffected at all measured Ra.

The probability density functions (PDFs) of the temperature fluctuations of the plates $T_b(t)$ and $T_t(t)$ are evaluated using the signal from the fast-responding diodes $\mathrm{T_{b3}}$ and $\mathrm{T_{t3}}$ (see Fig. 1) with and without the PID control of the bottom plate temperature. All measured PDFs of the fluctuating $T_b(t)$ and $T_t(t)$ about mean temperatures $\langle T_b\rangle$ and $\langle T_t\rangle$ are approximately symmetric and of Gaussian shape, see Fig. 2. We have chosen two examples of Ra belonging to different $\mathrm{Nu(Ra)} \propto \mathrm{Ra}^\gamma$ scaling, the lower one in the range of $\gamma \approx 2/7$; the upper one above the crossover to $\gamma \approx 1/3$ [7, 19]. For all investigated Ra, the PID control of the bottom plate temperature results in significant narrowing of the bottom plate PDFs, while the PDFs measured at the top plate are not appreciably affected.

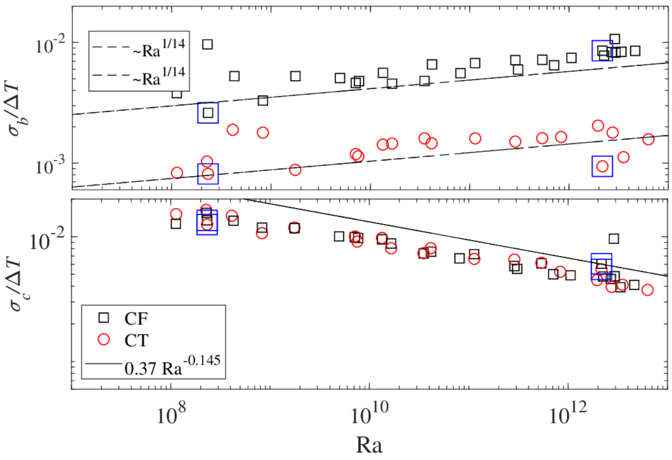

Fig. 4: Top panel shows the mean value of the temperature fluctuations σ_b measured by a diode T_{b3} mounted on the outer side of the bottom plate, normalized by ΔT, plotted versus Ra for CF BC (black open squares) and for the case of PID-controlled T_b; CT BC (red open circles). The dashed lines indicate the slope of $\mathrm{Ra}^{1/14}$. Bottom panel displays the mean of the temperature fluctuations $\sigma_c/\Delta T$ measured by a small Ge sensor No 7 in the centre of the RBC cell for CF BC (black open squares) and for the case of PID-controlled T_b; CT BC (red open circles). The solid line represents the the best fit through the same data measured by Niemela *et al.* [28]: $\sigma/\Delta T = 0.37\mathrm{Ra}^{-0.145}$. Large blue square symbols highlight cases shown in Figs. 2 and 3.

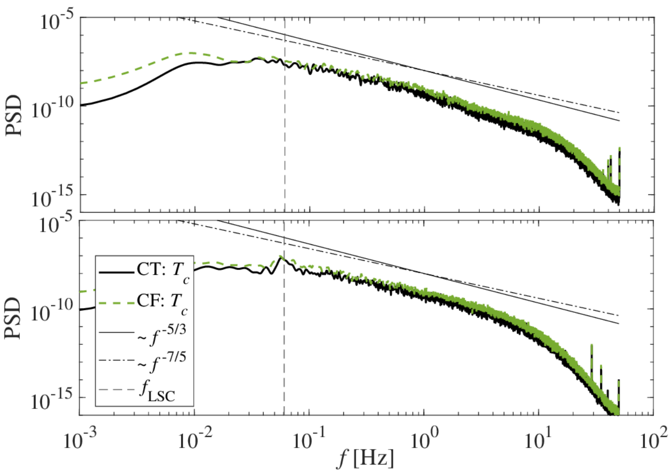

Fig. 5: PSDs of the temperature fluctuations in the bulk RBC at Ra= 2.2×10^{12} for CF (dashed green lines) and CT-like (solid black lines) BC at the bottom plate. The PSD in the top panel are measured by sensor No 7 in the geometrical centre of the cell, those in the bottom panel, displaying the LSC peak at 0.06 Hz, by sensor No 1, 20 mm from the sidewall. The lines represent the slopes of Bolgiano and Obukhov-Corrsin scaling with, respectively, -7/5 and -5/3 roll-off exponents.

It is instructive to calculate and compare the power spectral density (PSD) of temperature fluctuations for the PID control on and off. As shown in Fig. 3, the PID control results in significant depletion of PSDs at low frequencies below about $0.4 - 0.7$ Hz, while faster temperature fluctuations of the bottom plate are hardly affected. The top plate PSDs remain at all measured Ra entirely unaffected.

The top panel of Fig. 4 displays the mean value of the temperature fluctuations σ_b measured by a diode T_{b3} normalized by ΔT, plotted versus Ra. While $\sigma_b/\Delta T$ slightly increases with increasing Ra (approximately $\propto \mathrm{Ra}^{1/14}$) for both CF and CT BC on the bottom plate, the imposed CT BC reduces its numerical values by a factor of about four. The same quantity, $\sigma/\Delta T$ in the top and bottom Cu plates in rectangular RBC cells of various sizes was measured at ambient temperatures under CT and CF BC in a similar study by Huang *et al.* [29], by using H_2O as the working fluid. It is remarkable that Fig. 1d of Ref. [29] clearly shows, for both the top and bottom plates, the opposite tendency in the $\sigma/\Delta T$ versus Ra dependence. We speculate that this apparent discrepancy could be explained by very different dynamic characteristics of cryogenic He and ambient temperature H_2O turbulent RBC experiments, as some of them differ by orders of magnitude - see Table 1.

Let us now discuss the main issue of this study: what changes, if any, are experimentally observed in the *bulk* of the RBC flow as a consequence of distinctly different BC at the bottom plate. We start with the same quantity, $\sigma/\Delta T$, but measured now not at the plates but in the centre of the RBC cell. The bottom panel of Fig. 4 shows that, contrary to the situation at the bottom plate, $\sigma_c/\Delta T$ in the centre is not appreciably sensitive to the change of BC at the bottom plate and scales $\propto \mathrm{Ra}^{-1/7}$, and behaves in accord with our previous studies [26] performed in the RBC Brno cell as well as with the seminal work of Niemela *et al.* [28] quoting the best fit $\sigma/\Delta T = 0.37\mathrm{Ra}^{-0.145}$, shown in the bottom panel of Fig. 4 as a solid line for comparison.

Fig. 5 shows examples of PSDs of the temperature fluctuations in the centre of the RBC cell (top) and at the mid plane 20 mm from the sidewall (bottom) measured at Ra $= 2.2 \times 10^{12}$. As it is typical for confined high Ra RBC flow, the PSD measured near the sidewall displays the LSC peak, in this case at 0.06 Hz, which is used to calculate the mean velocity of the LSC, the "wind". In accord with [28], the PSD are consistent with a roll-off rate of $-7/5$ for low frequencies where Bolgiano scaling seems appropriate, whereas for higher frequencies, the classical Obukhov-Corrsin scaling with the roll-off exponent $-5/3$ appears more appropriate. The key observation is that at all investigated Ra, except for slight depletion at very low frequencies below 0.02 Hz, the bulk PSD of the temperature fluctuations are unaffected by the imposed change of BC on the bottom plate.

In our previous work [26] we discussed in detail several definitions of Reynolds numbers, evaluated them using the "standard" CF BC and directly compared them with results published by other authors. Here we utilize temperature fluctuations measured by various single and pairs of Ge sensors in the cell (see Fig. 1) and compare Reynolds

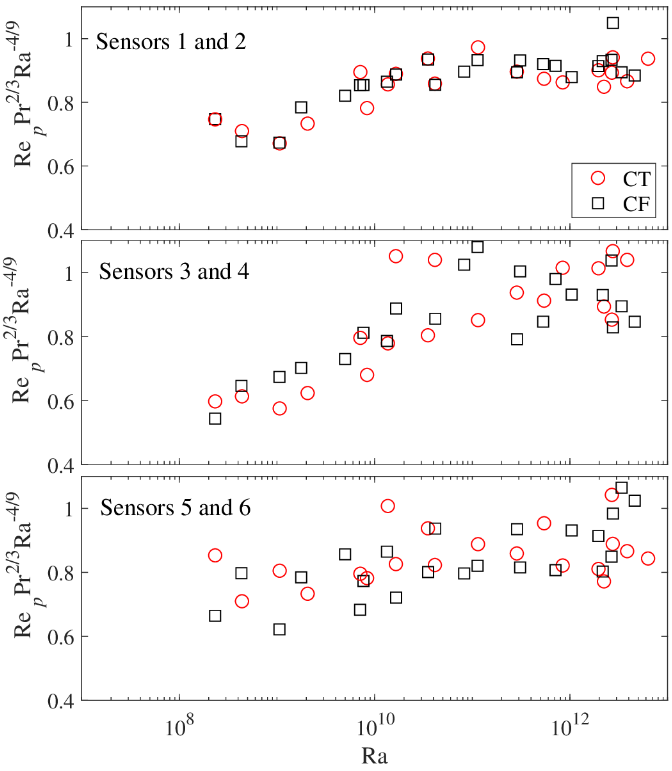

Fig. 6: Reynolds number Re_p calculated using temperature signals from pairs of vertically spaced Ge sensor as indicated, plotted in a compensated form versus Ra.

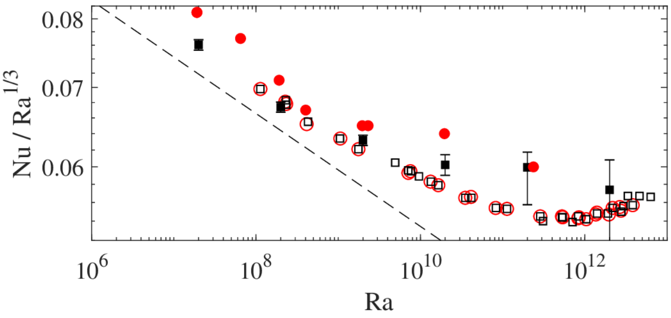

Fig. 7: Compensated Nu plotted versus Ra for "standard" RBC generation (CF BC on the bottom plate, open squares) and for the case of PID control of temperature of the bottom plate (BC closer to CT, open red circles). The data series have been measured under the same experimental conditions and only the same basic corrections, due to adiabatic gradient and parasitic heat leak have been applied. Also shown are CF (filled black squares) and CT (filled red circles) numerical data for $\Gamma = 1/2$ and Pr=0.7 [6], see the text for details. The dashed line indicates the slope $\mathrm{Nu} \propto \mathrm{Ra}^{2/7}$.

numbers and their scaling with Ra for CF and CT BC at the bottom plate.

In the case of one probe measurement, the characteristic frequency f_0 determined from the peak of the near-wall PSD of the temperature fluctuations (an example shown at the bottom of Fig. 5) is used in definition of the frequency-based Reynolds number $\mathrm{Re}_{f0} = 2L^2 f_0/\nu_f$. We already discussed that the near-wall PSD remain unaffected by the change of the BC at the bottom plate, so Re_{f0} is unaffected, too.

In the case of two probe measurements, the simplest approach relies on the Taylor's frozen flow hypothesis and uses the time delay between temperature fluctuation records at two nearby sensors spaced by a vertical distance d, which determines the mean velocity U_p. The corresponding Reynolds number is defined as $\mathrm{Re}_p = LU_p/\nu_f$. In [26] we claimed observation of a crossover in the slope of Re_p with Ra around 10^{10} (complementary to the crossover in $\mathrm{Nu(Ra)} \propto \mathrm{Ra}^{\gamma}$ scaling from $\gamma \approx 2/7$ to $\gamma \approx 1/3$). We confirm this crossover for both CF and CT BC on the bottom plate; it is clearly seen in the compensated plot of $\mathrm{Re}_p\mathrm{Pr}^{2/3}/\mathrm{Ra}^{4/9}$ versus Ra, displayed in the top panel of Fig. 6. We have evaluated Reynolds numbers according to all definitions discussed in our previous work [26] and found them hardly affected by the changing CF and CT BC at the bottom plate. The Re_p data shown in the top panel of Fig. 6 were evaluated using sensors 1 and 2 (see Fig. 1) which in all experimental runs displayed very rare reversals of the LSC direction: 1.5 ± 0.2 (1.8 ± 0.3) reversals/hour for CF (CT) cases, as the sensors presumably lied near the main LSC plane. The data in the middle and bottom panels are from the sensor pairs 3, 4 and 5, 6, which lied in the plane perpendicular to the previous pair and experienced more frequent reversals of an auxiliary flow: 9.7 ± 0.4 (9.9 ± 0.4) reversals/hour for CF (CT) cases. Similar situation was observed by Sun *et al.* [30] using PIV combined with thermometry. More detailed statistical study of LSC reversals as well as analysis employing the so-called elliptic approximation in evaluation of Re will be published elsewhere.

Last but not least we now discuss the essential feature of turbulent RBC flow - its ability to transfer heat, usually expressed in dimensionless form, by the Nusselt number. The key question is: Does Nu depend on boundary conditions? Our experimental answer is provided in a graphical form in Fig. 7: Changing CF to CT BC at the bottom plate does not appreciably change the heat transfer efficiency, at least over the investigated range $10^8 < \mathrm{Ra} < 3 \times 10^{12}$. Being fully aware of the fact that accurate determination of the Nu(Ra) dependence involves application of various corrections to the raw data, we do not claim here the absolute accuracy of the displayed compensated Nu(Ra) dependence. We stress, however, that the only difference between the displayed two sets of data is the *in situ* change of CF (or rather CF-like) and CT (or rather CT-like) BC at the bottom plate as discussed in detail above.

This experimental result can be compared with complementary numerical studies. Following the earlier simulations of Amati *et al.* [31], Verzicco & Sreenivasan [5], and 2D simulations of Johnston & Doering [25], Stevens, Lohse & Verzicco [6] performed thorough 3D simulations